A two-field modified lagrangian formulation for robust simulations of extrinsic cohesive zone models

Fabien Cazes, Michel Coret, Alain Combescure

A two-field modified Lagrangian formulation for robust simulations of extrinsic cohesive zone models

F. Cazes, M. Coret, A. Combescure

Abstract This paper presents the robust implementation of a cohesive zone model based on extrinsic cohesive laws (i.e. laws involving an infinite initial stiffness). To this end, a two-field Lagrangian weak formulation in which cohesive tractions are chosen as the field variables along the crack's path is presented. Unfortunately, this formulation cannot model the infinite compliance of the broken elements accurately, and no simple criterion can be defined to determine the loading–unloading change of state at the integration points of the cohesive elements. Therefore, a modified Lagrangian formulation using a fictitious cohesive traction instead of the classical cohesive traction as the field variable is proposed. Thanks to this change of variable, the cohesive law becomes an increasing function of the equivalent displacement jump, which eliminates the problems mentioned previously. The ability of the proposed formulations to simulate fracture accurately and without field oscillations is investigated through three numerical test examples.

Keywords Failure · Finite element · Lagrangian multiplier

1 Introduction

According to Griffith's theory [1], the fracture of a brittle material can be modeled by introducing a discontinuity into the structure if the work of some forces acting between the two sides of the crack is taken into account in the global energy balance. In that early study of fracture, the zone where the two sides of the crack interact was assumed to be small with regard to the size of the structure, which was justified by the brittleness of the material being studied. More recent models have been proposed taking into account the interaction forces between the two sides of the crack, i.e. the cohesive forces, not only in the energy balance of the structure, but also in the equilibrium equations of the mechanical problem. This improvement to Griffith's original model leads to a more accurate estimation of the mechanical fields near the crack's tip [2,3] and enables the application of cracking models to non-brittle materials, such as ductile materials [4] and quasi-brittle materials [5]. These models, generally designated as cohesive zone models (CZM), were cast in a sound thermodynamic framework in [6]. The behavior of the cohesive zone is usually described by a function, called a cohesive law, which provides the relation between the cohesive traction and the displacement jump.

Using the finite element method, the numerical implementation of CZM can be carried out in different ways. If the crack's path is known beforehand, zero-width elements, called cohesive elements, can be introduced at the interfaces between a selection of volume elements [5,7,8]. Cohesive elements can also be introduced at the interfaces between all the volume finite elements if the crack's path is unknown; this approach is most often used in the case of dynamic calculations [9]. The embedded finite element method (E-FEM) [10,11] and the eXtended finite element method (X-FEM) were proposed in order to reduce the mesh dependency of the crack paths. One should note that the X-FEM was first introduced for Griffith models [12,13], but is also compatible with CZM [14–16]. This paper deals with standard cohesive elements placed either between a selection of volume finite elements or between all the finite elements of the mesh.

The earliest formulation involving cohesive elements was a single-field displacement-based formulation [8]. This formulation is limited to cohesive laws with strictly positive

F. Cazes (✉) · M. Coret · A. Combescure
Université de Lyon, CNRS, INSA-Lyon, LaMCoS UMR5259,
69621 Villeurbanne, France
e-mail: fabien.cazes@gmail.com

initial compliance, i.e. intrinsic laws, because the existence of an infinite stiffness at an integration point of the cohesive zone would lead to infinite terms in the global system of equations. The additional compliance introduced by CZM may be physically motivated, e.g. considering molecular forces of cohesion [3] or due to the finite thicknesses of pre-existing interfaces [17]. Unfortunately, in the case of an intrinsic law, as established in previous works on the initiation of cohesive zones [18], the initiation stress is equal to zero, which means that cracks should appear in all the regions of the domain in which the stress tensor is not equal to zero. This theoretical difficulty is partially eliminated in numerical calculations using cohesive elements because a crack can appear only where cohesive elements have been introduced, but a spurious compliance is still introduced into the structure before the physical crack initiation criterion is met. This additional compliance can be reduced by means of a penalty method which consists in choosing a large initial slope, but this can lead to numerical instabilities, as can be seen in [19] for static problems and in [20] for dynamic problems.

These problems, which are related to the initial compliance of the cohesive elements, can be solved using other formulations which are compatible with extrinsic cohesive laws. In [21], a three-field augmented Lagrangian formulation is used with the displacement as the field variable for the continuous part of the domain, and both the cohesive traction and the displacement jump as the field variables for the discontinuous part of the domain. In [22] and [23], an extrinsic law is implemented using a two-field truly mixed formulation with the displacement and the stress over the entire domain as the field variables. Both these mixed formulations can be used to implement extrinsic CZM, but the discretization must be chosen carefully because the *inf-sup* condition [24,25] must be satisfied in order to avoid spurious oscillations of the field variables. For the augmented Lagrangian formulation, the order of the volume elements must be higher than that of the cohesive elements. For the truly mixed formulation, a Johnson-Mercier element [26] is used in [23] to ensure the smoothness of the numerical results. According to [27], an alternative would be to force the two sides of the crack to remain in contact prior to initiating the cohesive zone using the discontinuous Galerkin method (or Nitsche's method).

When standard displacement-based formulations are used with extrinsic cohesive laws, a way to circumvent the problem of the infinite initial stiffness is to introduce the cohesive elements only at the place where the crack is initiated, e.g. using extended finite elements. In this case, the size of the system of equations increases while the crack propagates. This method requires to recover the cohesive tractions at the crack's tip to evaluate the propagation criterion. To this end, a non-local averaging procedure [14] can be defined: the values of the stress in the volume elements surrounding the crack are used to approximate the cohesive stress at the crack tip. Nevertheless, when contact between the two sides of the crack is considered, it is still usefull to use a mixed formulation in combination with the X-FEM [28] to evaluate the contact condition precisely. In this paper, cohesive elements that are introduced from the beginning of the calculation between volume elements of the mesh will be used, which avoids changing the discretization while the crack propagates, and avoids to compute non-local stresses at the crack tip as the initiation criterion is evaluated directly at the integration points of the cohesive elements.

In this paper, we use a two-field coupled formulation in which the field variables are the displacement in the volume and the cohesive traction along the crack's path. The advantage of this formulation is its simplicity because the cohesive tractions along the crack can be viewed as standard Lagrange multipliers. It is compatible with the infinite initial stiffness of extrinsic cohesive zones as well as with the use of linear volume elements and linear cohesive elements if the crack's path is known beforehand. Unfortunately, this formulation is unable to deal with broken cohesive elements unless they are deleted during the calculation, and it is relatively difficult to differentiate between a loading state and an unloading state when updating the internal variables of the cohesive zone because the cohesive traction decreases in both cases. The main contribution of this paper consists in showing that both situations can be handled thanks to a change of variable which modifies the cohesive traction in the local equations of the problem. Then, the cohesive law is replaced by an increasing law linking a fictitious equivalent cohesive traction to the equivalent displacement jump of the discontinuity. This method was presented in [29], but only for the case of straight crack propagation. This paper also addresses the case of an a priori unknown crack's path by introducing cohesive elements at the interfaces between all the volume elements of the mesh. In Sect. 2, we design the CZM in order to reproduce the behavior of a smeared crack model approximately. In Sect. 3, we present the cohesive-stress-based Lagrangian formulation along with a numerical application to the case of straight crack propagation. In Sect. 4, we introduce the concept of fictitious cohesive traction and use it as a field variable in the second formulation (the modified Lagrangian formulation). The implementation of this formulation is presented in detail and applied both to a straight crack propagation and to the case of a crack whose path is unknown.

2 CZM

Development using a smeared crack model Let us consider a two-dimensional domain Ω bounded by Γ and filled with an elastic and isotropic material. A displacement vector $\boldsymbol{u}$ is defined within Ω such that

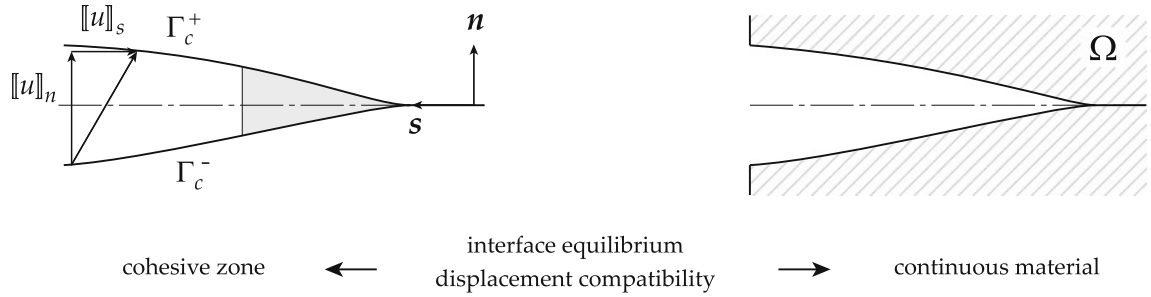

Fig. 1 Decomposition of the *volume/interface* problem

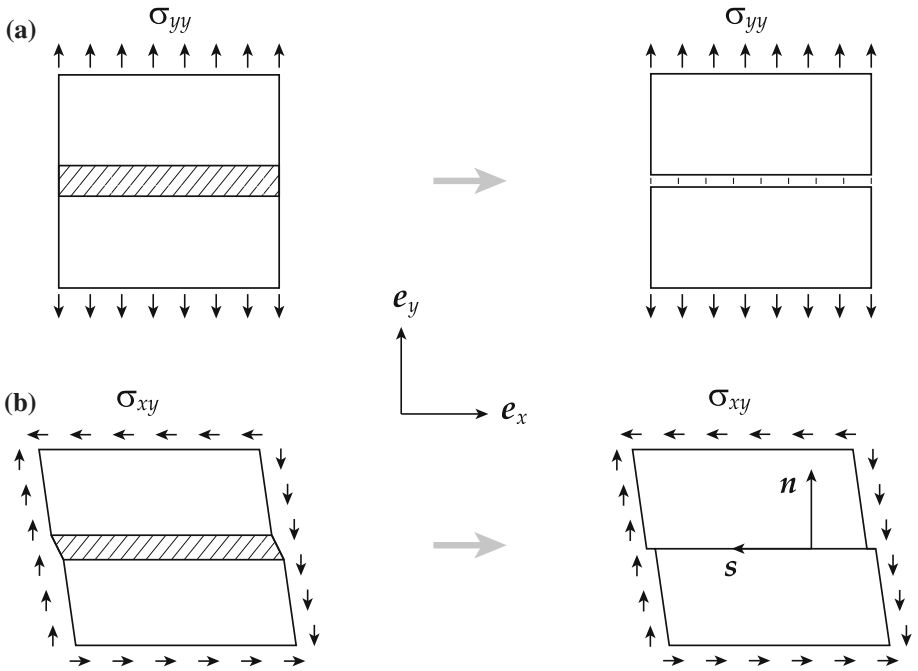

Fig. 2 Construction of the CZM by analogy with a smeared crack model

$$\boldsymbol{u} = \begin{bmatrix} u_x & u_y \end{bmatrix}^T, \tag{1}$$

where u_x and u_y are the components of the displacement in the $(\boldsymbol{e}_x, \boldsymbol{e}_y)$ basis. Ω is cut by an interface Γ_c defined in Fig. 1. Along Γ_c, the displacement jump vector $[\![\boldsymbol{u}]\!]$ and the cohesive traction vector $\boldsymbol{t}$ are defined such that

$$[\![\boldsymbol{u}]\!] = \begin{bmatrix} [\![u]\!]_n & [\![u]\!]_s \end{bmatrix}^T, \tag{2a}$$

$$\boldsymbol{t} = \begin{bmatrix} t_n & t_s \end{bmatrix}^T, \tag{2b}$$

where $[\![u]\!]_n$ and $[\![u]\!]_s$ are the components of the displacement jump and t_n and t_s the components of the cohesive traction in the local basis $(\boldsymbol{n}, \boldsymbol{s})$. The behavior of the cohesive zone is given by the equation

$$[\![\boldsymbol{u}]\!] = c_{eq}\, \boldsymbol{C}_0\, \boldsymbol{t}, \tag{3}$$

where c_{eq} is an equivalent compliance and $\boldsymbol{C}_0$ a matrix defined as:

$$\boldsymbol{C}_0 = \begin{bmatrix} (1 - c_0) & 0 \\ 0 & \beta \end{bmatrix}. \tag{4}$$

c_0 is a contact indicator defined along Γ_c and equal to 1 if the two borders of the discontinuity are in contact and to 0 otherwise, and β is a material parameter linking the compliances of the cohesive zone in shear and in traction. The CZM is designed to reproduce the behavior of a smeared crack model [30] in which the internal damage variable D is homogeneous within a band of width h. In order to determine the relation between the traction behavior and the shear behavior in plane stress, we consider successively the two simple solicitations illustrated in Fig. 2. For the first solicitation (traction), the stress components are:

$$\sigma_{xx} = 0, \quad \sigma_{yy} = \sigma, \quad \sigma_{xy} = 0, \tag{5}$$

and for the second solicitation (shear), the stress components are:

$$\sigma_{xx} = 0, \quad \sigma_{yy} = 0, \quad \sigma_{xy} = \sigma, \tag{6}$$

where σ is a homogenous, positive scalar quantity defined over Ω. Using these two solicitations, we obtain the following two equations, respectively:

$$\frac{[\![u]\!]_n}{h} + \frac{t_n}{E} = \frac{t_n}{(1-D)\,E}, \tag{7a}$$

$$\frac{[\![u]\!]_s}{h} + \frac{t_s}{G} = \frac{t_s}{(1-D)\,G}, \tag{7b}$$

where E is the material's Young's modulus, and G the shear modulus defined as $G = E/(2\,(1+\nu))$. According to Eqs. (3) and (4),

$$\frac{[\![u]\!]_s}{[\![u]\!]_n} = \beta\,\frac{t_s}{t_n}. \tag{8}$$

Besides, Eqs. (7a) and (7b) lead to:

$$\frac{[\![u]\!]_s}{[\![u]\!]_n} = \frac{E}{G}\,\frac{t_s}{t_n}, \tag{9}$$

where ν is the material's Poisson's ratio. Considering Eqs. (8) and (9), the identification of β with E/G leads to the following value of β:

$$\beta = 2\,(1+\nu). \tag{10}$$

Note that in the plane strain case the Young's modulus E should be replaced in Eq. (9) by a modified value $\bar{E} = E/(1-\nu^2)$, leading to the definition a modified parameter $\bar{\beta}$ such that:

$$\bar{\beta} = \frac{2}{1-\nu}. \tag{11}$$

It should be noted, that the cohesive law may also be derived according to the damage model that is defined within the band [31], which is out of the scope of the present paper.

Equivalent cohesive traction and displacement jump As in Camacho and Ortiz's model [32], both an equivalent cohesive traction and an equivalent displacement jump are defined along the crack's path Γ_c. The equivalent stress, denoted t_{eq}, satisfies:

$$t_{eq} = \sqrt{(t_n^+)^2 + \gamma^2\,t_s^2}\,, \tag{12}$$

where γ is a material parameter and t_n^+ denotes the positive part of t_n. The initiation occurs when the equivalent cohesive traction reaches a critical value denoted t_c. Figure 3 shows the corresponding initiation yield surface. The equivalent displacement jump $[\![u]\!]_{eq}$ is defined as

$$[\![u]\!]_{eq} = c_{eq}\;t_{eq}. \tag{13}$$

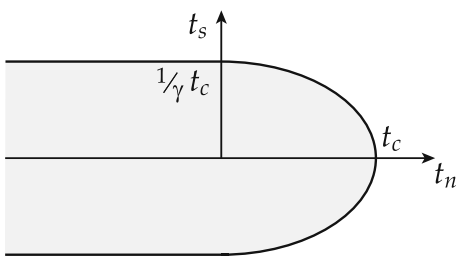

Fig. 3 The initiation yield surface in the cohesive traction space

Using Eqs. (8), (9), and (12), this leads to the following expression of $[\![u]\!]_{eq}$:

$$[\![u]\!]_{eq} = \sqrt{[\![u]\!]_n^2 + \frac{\gamma^2}{\beta^2}\,[\![u]\!]_s^2}\,. \tag{14}$$

The maximum value of $[\![u]\!]_{eq}$ over time is stored in the variable κ defined as:

$$\kappa = \max_t\big([\![u]\!]_{eq}\big). \tag{15}$$

Using CZM, it is common to enforce that the total surface cracking energy G_c is independent of the loading history of the cohesive zone [32,33]. Accordingly, the following condition is assumed (see justification in Appendix A):

$$\gamma = \sqrt{\beta}. \tag{16}$$

3 The Lagrangian formulation

In this section, we define a weak formulation, called Lagrangian Formulation, in which the unknown fields are the displacement field $\boldsymbol{u}$ over Ω and the cohesive traction field $\boldsymbol{t}$ along Γ_c. This formulation will be the basis of an improved formulation, called the Modified Lagrangian Formulation, using a modified definition of the cohesive traction to improve the robustness of the calculations. In Sect. 4, we will show that this formulation can be seen as a limit case of the proposed modified Lagrangian formulation.

3.1 The weak formulation

Since the boundary conditions are limited to prescribed forces along the boundary Γ of domain Ω, the equilibrium of the structure can be written as:

$$\int_\Omega \nabla^s(\boldsymbol{u}^*)^T\boldsymbol{\sigma}\;d\Omega + \int_{\Gamma_c} [\![\boldsymbol{u}^*]\!]^T\boldsymbol{t}\;d\Gamma_c = \int_\Gamma \boldsymbol{u}^{*T}\boldsymbol{F}_d\;d\Gamma, \quad \forall\,\boldsymbol{u}^*\in\mathcal{F}, \tag{17}$$

where $\mathcal{F}$ denotes the space of the continuous and regular displacement vectors defined over Ω, ∇^s is the symmetrical gradient operator, $[\![.]\!]$ the displacement jump operator (including its projection onto the local basis), $\boldsymbol{\sigma}$ the stress vector, $\boldsymbol{u}$ the displacement vector, and $\boldsymbol{F}_d$ the vector of the prescribed external forces. According to Eq. (17), a weak formulation is defined with field variables $\boldsymbol{u}$ over Ω and $\boldsymbol{t}$ along Γ_c. The space of the cohesive traction fields, defined along Γ_c, is denoted $\mathcal{G}$. These fields may be continuous or discontinuous at the junction between cohesive elements depending on the approximation used. (A continuous approximation will be assumed for examples A and B, and a discontinuous approximation will be assumed for example C.) Then, according to Eq. (17), we have the following weak formulation:

$$\mathcal{A}(\boldsymbol{u}^*) + \mathcal{B}(\boldsymbol{u}^*) + \mathcal{C}(\boldsymbol{t}^*) = \mathcal{D}(\boldsymbol{u}^*), \quad \forall\, (\boldsymbol{u}^*, \boldsymbol{t}^*) \in (\mathcal{F}, \mathcal{G}), \tag{18}$$

with

$$\mathcal{A}(\boldsymbol{u}^*) = \int_\Omega \boldsymbol{\nabla}^s(\boldsymbol{u}^*)^T\, \boldsymbol{\sigma}(\boldsymbol{u})\, d\Omega, \tag{19a}$$

$$\mathcal{B}(\boldsymbol{u}^*) = \int_{\Gamma_c} [\![\boldsymbol{u}^*]\!]^T\, \boldsymbol{t}\, d\Gamma_c, \tag{19b}$$

$$\mathcal{C}(\boldsymbol{t}^*) = \int_{\Gamma_c} \boldsymbol{t}^{*T} \big([\![\boldsymbol{u}]\!] - [\![\boldsymbol{u}]\!](\boldsymbol{t}) \big)\, d\Gamma_c, \tag{19c}$$

$$\mathcal{D}(\boldsymbol{u}^*) = \int_\Gamma \boldsymbol{u}^{*T} \boldsymbol{F}_d\, d\Gamma. \tag{19d}$$

In Eq. (19a), $\boldsymbol{\sigma}(\boldsymbol{u})$ designates the stress calculated using the behavior of the continuous elastic material and the displacement field. In Eq. (19c), the term $\mathcal{C}$ introduces the behavior of the cohesive zone into the coupled formulation and expresses the gap between the displacement jump $[\![\boldsymbol{u}]\!]$ calculated according to the displacement field of the continuous material and the displacement jump $[\![\boldsymbol{u}]\!](\boldsymbol{t})$ calculated according to the cohesive law and the cohesive traction $\boldsymbol{t}$.

Remark If one compares the Lagrangian formulation to a truly mixed formulation applied to a problem with a cohesive crack [22,23], one can observe the following differences:

- The stress (defined over Ω) is a field variable of the Truly Mixed Formulation, whereas the cohesive traction (defined along Γ_c) is a field variable of the Lagrangian formulation.
- Both formulations use a compliance operator to describe the behavior of the cohesive zone, but the truly mixed formulation also uses a compliance operator to describe the behavior of the continuous material, whereas the Lagrangian formulation uses a stiffness operator.
- The truly mixed formulation is obtained from the Hellinger-Reissner principle, whereas the Lagrangian formulation is a displacement-based formulation combined with an approximation of the cohesive traction field which plays the role of a Lagrange multiplier. Also, according to the definition provided in [34], the Lagrangian formulation is a coupled formulation which can be considered to be a mixed formulation only until the crack initiation criterion is met at all the integration points of the crack (see Appendix E).

Equation (19) is discretized in the usual finite element way. The discretized equations for this formulation are not shown in detail, but they will be given in Sect. 4 for the modified Lagrangian formulation. Since the behavior of the cohesive zone is nonlinear, the numerical implementation uses an iterative-incremental approach in which the loading factor increments are provided by a continuation method.

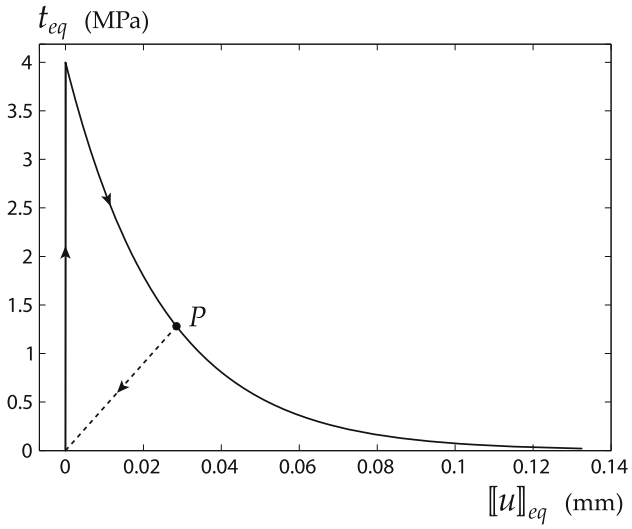

Fig. 4 Test example A: exponential cohesive law

3.2 Test example A

The first test example concerns the analysis of a rectangular slab of width $L_1 = 300\,\text{mm}$ and height $L_2 = 200\,\text{mm}$ (see Fig. 5). A zero-width horizontal interface cuts through the middle of this slab. The material is elastic and isotropic, and plane stress conditions are assumed. Figure 4 shows the exponential cohesive law being used. According to this cohesive law, the equivalent compliance c_{eq} satisfies:

$$c_{eq}(\kappa) = \frac{\kappa}{t_c\, \exp(-b\,\kappa)}, \tag{20}$$

where t_c and b are material parameters. When loading is applied, the equivalent cohesive traction is given by

$$t_{eq} = t_c\, \exp(-b\, [\![u]\!]_{eq}). \tag{21}$$

Using the notations of Fig. 5, the loading consists of prescribed displacements denoted $\boldsymbol{u}_d$ applied along $\Gamma_1 = [AB] \cup [CD]$, which satisfy

$$\boldsymbol{u}_d = \lambda\, \boldsymbol{u}_1, \quad \text{along } \Gamma_1, \tag{22}$$

where λ represents the loading factor, and $\boldsymbol{u}_1$ is defined such that $\boldsymbol{u}_1 = \boldsymbol{0}$ along $[AB]$ and

$$\boldsymbol{u}_1 = \begin{bmatrix} 0 & 10 - 0.02\,x & \end{bmatrix}^T \text{mm}, \quad \text{along } [CD] \tag{23}$$

using the referential $(A, \boldsymbol{e}_x, \boldsymbol{e}_y)$. The material parameters were chosen to be $E = 40\,\text{GPa}$ (Young's modulus), $\nu = 0.2$ (Poisson's ratio), $t_c = 4\,\text{MPa}$, $\beta = 2.4$ (to be consistent with the value of Poisson's ratio), $\gamma = \sqrt{\beta}$, and $b = 40$ (leading to

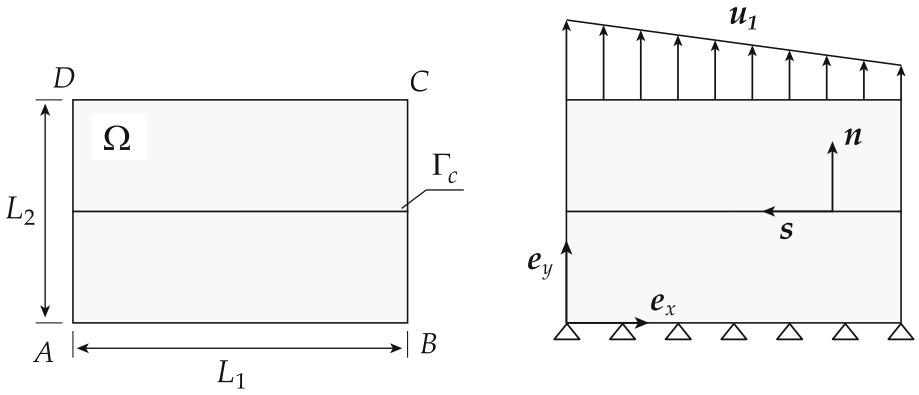

Fig. 5 Test example A: geometry and boundary conditions

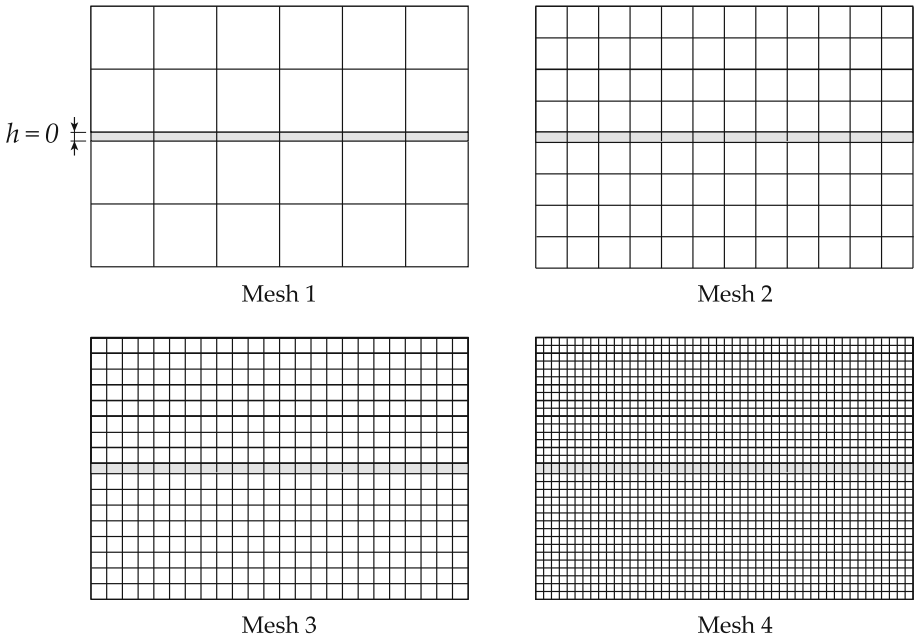

Fig. 6 Test example A: the meshes of density levels 1 to 4

$G_c = 0.1\,\mathrm{N.mm^{-1}}$). Figure 6 shows the 4 rectangular meshes which were used for the calculations. The mesh of density level i consisted of $6\times4^{(i-1)}$ volume elements and $3\times2^{(i-1)}$ interface elements. The volume elements were linear quadrilaterals with 4 nodes and 4 Gauss integration points, and the interface elements were linear elements with two nodes and two Newton-Cotes integration points. Starting from the beginning of the calculation, the cohesive elements were placed along the prescribed crack's path Γ_c shown in Fig. 5. Internal variables were used to define the decohesion state at the integration points. Figure 7 shows the norm F of the resultant of the forces applied to segment $[C\,D]$ as a function of the loading factor λ for the four meshes. One can observe that this curve converges when the mesh density increases.

3.3 Discussion

Influence of the spatial integration The quadrature used to perform numerical integrations along the crack's path must be chosen carefully. In general, Gauss quadrature is not used with displacement-based cohesive elements because it would lead to oscillations in the cohesive traction field. In [35], based on a study of Eigenmodes, it was shown that the use of Newton-Cotes points limits the oscillations of the cohesive traction field. The Lagrangian formulation also leads to better results when Newton-Cotes points are used. Figure 8 shows equivalent cohesive traction fields obtained using Newton-Cotes points and Gauss points for the same test (test example A and mesh density level 4). These plots show that Gauss points may lead to instabilities which can be avoided using Newton-Cotes points.

Advantages and limits of the formulation When a standard displacement-based formulation is used to implement cohesive elements, an artificial initial compliance has to be introduced in the constitive law of the discontinuity to avoid that very large (theoretically infinite) terms appear in the stiffness matrix. This leads to an ill conditioned stiffness. The Lagrangian formulation provides a solution

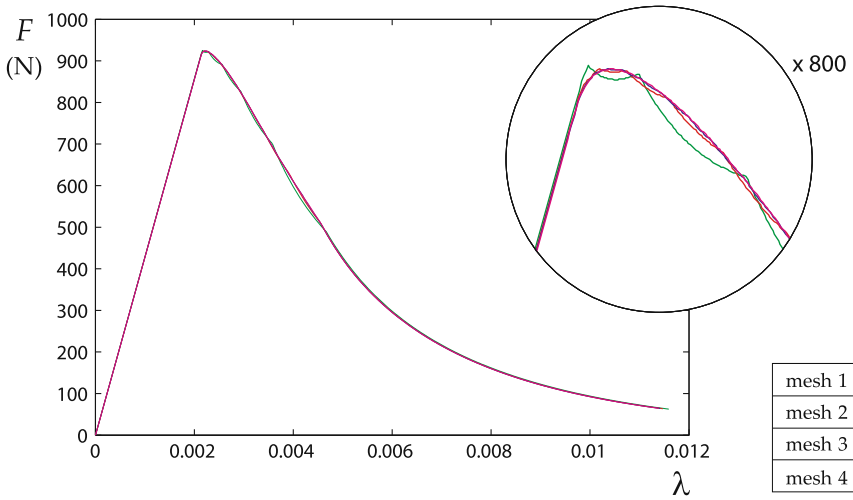

		number of volume elements	number of cohesive elements
mesh 1		24	6
mesh 2		96	12
mesh 3		384	24
mesh 4		1536	48

Fig. 7 Test example A: Superposition of the loading curves obtained with the 4 meshes

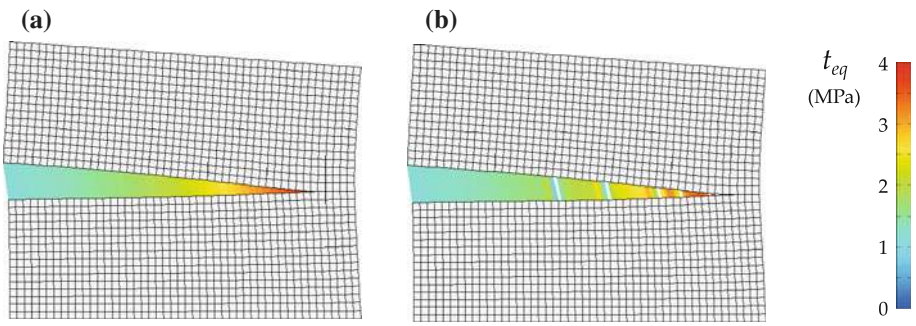

Fig. 8 Test example A: two equivalent stress fields obtained for mesh density level 4 using **a** Newton-Cotes points and **b** Gauss points (1,000× magnification)

to this problem, as a compliancy matrix is computed for the cohesive zone (infinite terms in the stiffness matrix of the displacement-based formulation becomes zero terms in the compliancy matrix of the Lagrangian formulation). On the other hand, a drawback of the Lagrangian formulation is that, if the cohesive zone breaks at an integration point, it becomes impossible to calculate the corresponding elementary compliance matrix because some of its terms go to infinity. This problem can be solved if one deletes the broken elements during the calculation. This solution was implemented by the authors, but the resulting computations were not robust. The numerical instabilities that were observed may come from the fact that the cohesive traction were not strictly equal to zero in an element when it was deleted. Another drawback is there is no available clear criterion to determine the loading state of the cohesive zone while the internal variables of the cohesive elements are being updated. Indeed, since the field variable is the cohesive traction along the crack's surface, the criterion for the evaluation of the loading state should be based on the cohesive traction field. Looking at point P in Fig. 4, one can observe that the equivalent cohesive traction decreases as well during loading and during unloading, so there is no obvious criterion based on the cohesive traction that enables one to distinguish between loading and unloading of the cohesive zone. In the remainder of the paper, in order to eliminate these difficulties, we propose an alternative formulation, called the modified Lagrangian formulation, in which a change of variable is used to substitute a fictitious cohesive traction $\boldsymbol{\zeta}$, which depends on both the cohesive traction and the displacement jump, for the cohesive traction $\boldsymbol{t}$ in the local equations of the problem.

4 The modified Lagrangian formulation

4.1 Quadratic cohesive law

To show the ability of the second formulation to deal with broken cohesive zones, a quadratic cohesive law will be used in the next two sample analyses (test examples B and C). This law is defined in such a way that when loading is applied the equivalent cohesive traction t_{eq} satisfies

$$t_{eq} = t_c - a\,[\![u]\!]_{eq} + b\,([\![u]\!]_{eq})^2, \tag{24}$$

with

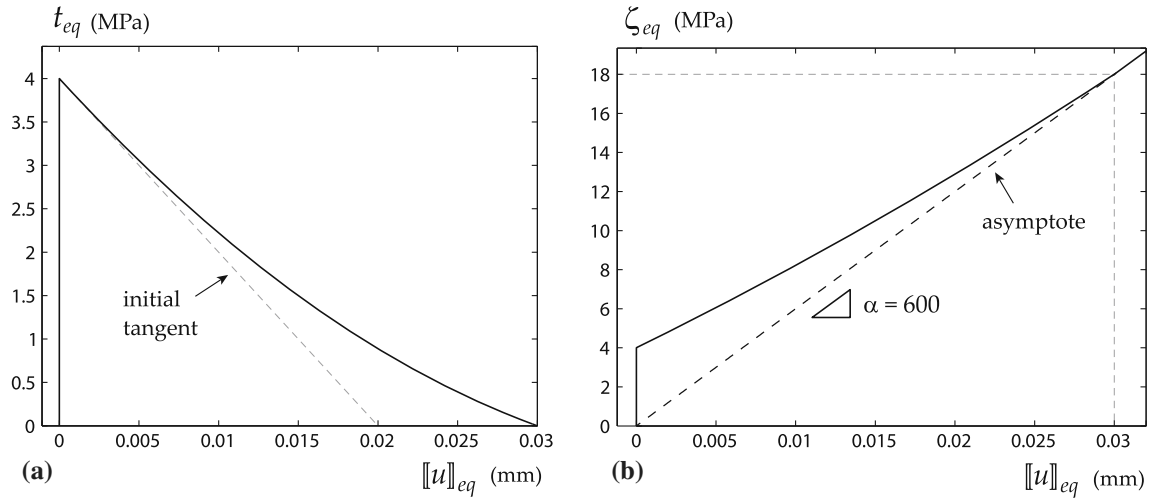

Fig. 9 **a** Quadratic cohesive law (used in test examples B and C and **b** the corresponding fictitious cohesive law

$$a = \frac{t_c}{[\![u]\!]_0}, \tag{25a}$$

$$b = t_c \left(\frac{1}{[\![u]\!]_0 \, [\![u]\!]_c} - \frac{1}{([\![u]\!]_c)^2} \right), \tag{25b}$$

where t_c, $[\![u]\!]_0$, and $[\![u]\!]_c$ are material parameters. The corresponding expression of the equivalent compliance c_{eq} is

$$c_{eq}(\kappa) = \frac{\kappa}{t_c - a\,\kappa + b\,\kappa^2}. \tag{26}$$

Figure 9a shows this quadratic cohesive law with the material parameters chosen as $t_c = 4\,\text{MPa}$, $\beta = 2.4$ (corresponding to Poisson's ratio $\nu = 0.2$), $\gamma = \sqrt{\beta}$, $[\![u]\!]_0 = 0.02\,\text{mm}$, and $[\![u]\!]_c = 0.03\,\text{mm}$ (leading to $G_c = 0.05\,\text{N mm}^{-1}$). These were the numerical parameters used in test examples B and C.

4.2 The fictitious cohesive traction

The difference between the Lagrangian formulation and the modified Lagrangian formulation is that in the latter the cohesive traction $\boldsymbol{t}$ is replaced in the local equations of the problem by a fictitious cohesive traction denoted $\boldsymbol{\zeta}$ and defined as

$$\boldsymbol{\zeta} = \boldsymbol{t} + \boldsymbol{\alpha}\,[\![\boldsymbol{u}]\!], \quad \text{along } \Gamma_c, \tag{27}$$

with,

$$\boldsymbol{\alpha} = \alpha \begin{bmatrix} 1 & 0 \\ 0 & 1/\beta \end{bmatrix}, \tag{28}$$

where α is a user-defined constant. The cohesive law is replaced by a law linking the equivalent displacement jump $[\![u]\!]_{eq}$ to a fictitious equivalent stress ζ_{eq} defined as

$$\zeta_{eq} = t_{eq} + \alpha\,[\![u]\!]_{eq}. \tag{29}$$

Let us note that making α equal to 0 reverts back to the original cohesive law. In practice, one chooses α to be large enough for the fictitious cohesive law to be an increasing function of the equivalent displacement jump. This property holds if α is chosen such that

$$\alpha = -k \, \min\left(\frac{\partial t_{eq}}{\partial \kappa} \right), \tag{30}$$

where k is a numerical parameter greater than 1. In the case of the quadratic law, according to (24), one obtains:

$$\alpha = k\,a, \quad \text{if } b > 0, \tag{31a}$$

$$\alpha = k\,(a - 2\,b\,[\![u]\!]_c), \quad \text{otherwise.} \tag{31b}$$

According to the numerical parameters given in Sect. 4.1, choosing $k = 3$ leads to $\alpha = 600\ \text{N mm}^{-3}$. The fictitious cohesive law corresponding to this value of α, shown in Fig. 9b, will be used in test examples B and C. There is no direct connection between ζ_{eq} and $\boldsymbol{\zeta}$, so the expression of ζ_{eq} is derived from Eqs. (12) and (14):

$$\zeta_{eq} = \sqrt{(t_n^+)^2 + \gamma^2 t_s^2} + \alpha \sqrt{[\![u]\!]_n^2 + \frac{\gamma^2}{\beta^2}\,[\![u]\!]_s^2}\,. \tag{32}$$

The fictitious equivalent compliance d_{eq} is defined as

$$[\![u]\!]_{eq} = d_{eq}\,\zeta_{eq}. \tag{33}$$

Therefore, according to Eqs. (13) and (29),

$$d_{eq} = \frac{c_{eq}}{1 + \alpha\,c_{eq}}. \tag{34}$$

Using Eqs. (3), (4), (27), and (28), one obtains

$$[\![\boldsymbol{u}]\!] = \frac{c_{eq}}{1 + \alpha\,c_{eq}}\,\boldsymbol{C}_0\,\boldsymbol{\zeta}, \tag{35}$$

and, thus,

$$[\![\boldsymbol{u}]\!] = d_{eq}\,\boldsymbol{C}_0\,\boldsymbol{\zeta}. \tag{36}$$

Remarks If the cohesive zone breaks, the equivalent compliance c_{eq} becomes infinite, which was one of the main problems associated with the implementation of the Lagrangian formulation (see Sect. 3.3). One should note that according to Eq. (35) a broken cohesive law leads to $d_{eq} = 1/\alpha$; therefore, the problem does not exist for the modified Lagrangian formulation.

The fact that the fictitious cohesive law is an increasing function of the equivalent displacement jump simplifies the determination of the state of the cohesive zone at a point. Indeed, if Eq. (30) is satisfied, the initiation of the cohesive zone can be evaluated using the criterion:

$$\max_t(\zeta_{eq}) > t_c, \tag{37}$$

the cohesive zone is in a loading state if:

$$\frac{d\zeta_{eq}}{dt} > 0, \tag{38}$$

the two sides of the crack are in contact if:

$$\zeta_n \leq 0, \tag{39}$$

and the cohesive zone is completely broken if:

$$\max_t\big(\zeta_{eq}\big) > \alpha\, [\![u]\!]_c. \tag{40}$$

4.3 The finite element problem

Weak formulation Now the field variables are the displacement $\boldsymbol{u}$ over the domain and the fictitious cohesive traction $\boldsymbol{\zeta}$ along the crack's path:

$$\begin{aligned}\mathcal{A}(\boldsymbol{u}^*) + \mathcal{B}(\boldsymbol{u}^*) + \mathcal{C}(\boldsymbol{\zeta}^*) &= \mathcal{D}(\boldsymbol{u}^*),\\ &\forall\, (\boldsymbol{u}^*, \boldsymbol{\zeta}^*) \in (\mathcal{F}, \mathcal{G}),\end{aligned} \tag{41}$$

with,

$$\mathcal{A}(\boldsymbol{u}^*) = \int_\Omega \boldsymbol{\nabla}^s(\boldsymbol{u}^*)^T \boldsymbol{\sigma}(\boldsymbol{u})\, d\Omega, \tag{42a}$$

$$\mathcal{B}(\boldsymbol{u}^*) = \int_{\Gamma_c} [\![\boldsymbol{u}^*]\!]^T (\boldsymbol{\zeta} - \boldsymbol{\alpha}\, [\![\boldsymbol{u}]\!])\, d\Gamma_c, \tag{42b}$$

$$\mathcal{C}(\boldsymbol{\zeta}^*) = \int_{\Gamma_c} \boldsymbol{\zeta}^{*T} \big([\![\boldsymbol{u}]\!] - [\![\boldsymbol{u}]\!](\boldsymbol{\zeta})\big)\, d\Gamma_c, \tag{42c}$$

$$\mathcal{D}(\boldsymbol{u}^*) = \int_\Gamma \boldsymbol{u}^{*T} \boldsymbol{F}_d\, d\Gamma. \tag{42d}$$

These equations are derived from the weak Eqs. (19) and (19) of the Lagrangian formulation using a change of variable to replace $\boldsymbol{t}$ by $\boldsymbol{\zeta}$ according to Eq. (27).

Remark If one compares the modified Lagrangian formulation with an augmented Lagrangian formulation (see [21]), one can observe the following differences:

- The augmented Lagrangian formulation is a three-field formulation (the displacement jump $[\![\boldsymbol{u}]\!]$ is also an unknown of the problem), whereas the modified Lagrangian formulation is a two-field formulation.
- The augmented Lagrangian formulation is obtained from a modification of the cohesive traction of the form $\boldsymbol{t} \leftarrow \boldsymbol{t} + r\,\big([\![\boldsymbol{u}]\!] - [\![\boldsymbol{u}]\!](\boldsymbol{t})\big)$, whereas the modified Lagrangian formulation is based on a change of variable which does not modify the mechanical problem.
- With the augmented Lagrangian formulation, the penalty parameter r is chosen to be large enough so that $[\![\boldsymbol{u}]\!] \approx [\![\boldsymbol{u}]\!](\boldsymbol{t})$, whereas the numerical parameter α used in the modified Lagrangian formulation is chosen such that the fictitious cohesive law is an increasing function of the equivalent displacement jump $[\![u]\!]_{eq}$.

Spatial discretization A first mesh is generated for domain Ω and a second mesh is generated for the discontinuity Γ_c. These two meshes do not need to be compatible, but this is the most natural choice. The nodal displacement components expressed in the $(\boldsymbol{e}_x, \boldsymbol{e}_y)$ basis form the column vector:

$$\boldsymbol{U} = \big[\, u_1^x \;\; u_1^y \;\; \ldots \;\; u_n^x \;\; u_n^y \,\big]^T, \tag{43}$$

where n is the number of nodes in the mesh of Ω. The nodal components of the fictitious cohesive traction expressed in the $(\boldsymbol{n}, \boldsymbol{s})$ basis form the column vector:

$$\boldsymbol{Z} = \big[\, \zeta_1^n \;\; \zeta_1^s \;\; \ldots \;\; \zeta_m^n \;\; \zeta_m^s \,\big]^T, \tag{44}$$

where m is the number of nodes in the mesh of Γ_c. The matrix of shape functions $\boldsymbol{E}$ is defined in order to approximate the cohesive traction $\boldsymbol{t}$ along an element:

$$\boldsymbol{t}(\xi) = \boldsymbol{E}(\xi)\, \boldsymbol{Z}_e, \tag{45}$$

where ξ is the abscissa of a point along a reference cohesive element and $\boldsymbol{Z}_e$ the restriction of $\boldsymbol{Z}$ to the degrees of freedom of a cohesive element. We also define an intermediary vector $[\![\boldsymbol{U}]\!]$, related to $\boldsymbol{U}$, which contains the components of the nodal displacement jumps in $(\boldsymbol{e}_x, \boldsymbol{e}_y)$:

$$[\![\boldsymbol{U}]\!] = \big[\, [\![u]\!]_1^x \;\; [\![u]\!]_1^y \;\; \ldots \;\; [\![u]\!]_{n_c}^x \;\; [\![u]\!]_{n_c}^y \,\big]^T, \tag{46}$$

where n_c is the number of nodes (possibly different from m) in the mesh of Ω which are adjacent to Γ_c. Matrix $\boldsymbol{T}$ defines the relation between the element vectors $[\![\boldsymbol{U}]\!]_e$ and $\boldsymbol{U}_e$:

$$[\![\boldsymbol{U}]\!]_e = \boldsymbol{T}\, \boldsymbol{U}_e. \tag{47}$$

Along Γ_c, the matrix of shape functions $\boldsymbol{C}$ and the change-of-base matrix $\boldsymbol{P}$ are defined such that $[\![\boldsymbol{u}]\!]$ takes the form

$$[\![\boldsymbol{u}]\!](\xi) = \boldsymbol{C}(\xi)\, \boldsymbol{P}\, [\![\boldsymbol{U}]\!]_e. \tag{48}$$

Matrix $\boldsymbol{C}$ depends on the approximation of the displacement field along the edges of the volume elements which are adjacent to the cohesive element being considered. For example, if the meshes of Ω and Γ_c are compatible and if linear volume elements are used, the displacement jump obtained with Eq. (48) is also linear along the cohesive elements. More details about the cohesive elements used in this paper can be found in Appendix D. Matrices $\boldsymbol{K}$, $\boldsymbol{J}$, $\boldsymbol{H}$ and vector $\boldsymbol{F}_{ext}$ are defined such that if the test field $\boldsymbol{\zeta}^*$ is equal to zero, then Eq. (41) takes the discrete and incremental form

$$\boldsymbol{U}^{*T}\big(\boldsymbol{K}-\boldsymbol{J}\big)\,\boldsymbol{dU}+\boldsymbol{U}^{*T}\boldsymbol{H}\,\boldsymbol{dZ}=\boldsymbol{U}^{*T}\boldsymbol{dF}_{ext},\quad \forall\,\boldsymbol{U}^{*}\in\bar{F},\quad (49)$$

where $\bar{F}$ denotes the set of the column vectors of dimension $2\,n$. $\boldsymbol{J}$ is obtained by assembling the elementary matrices $\boldsymbol{J}_e$ which satisfy

$$\boldsymbol{U}_e^{*T}\,\boldsymbol{J}_e\,\boldsymbol{dU}_e=\int_{\hat{\Gamma}_e^c}[\![\boldsymbol{u}^*]\!]^T\boldsymbol{\alpha}\;\boldsymbol{d}[\![\boldsymbol{u}]\!]\,J_c\,d\xi,\quad (50)$$

where $\hat{\Gamma}_e^c$ is the domain of a reference cohesive element and J_c is the Jacobian determinant of the transformation linking the reference element $\hat{\Gamma}_e^c$ to the physical element Γ_e^c. Consequently, one has:

$$\boldsymbol{J}_e=\int_{\hat{\Gamma}_e^c}\boldsymbol{T}^T\boldsymbol{P}^T\boldsymbol{C}^T\boldsymbol{\alpha}\;\boldsymbol{C}\;\boldsymbol{P}\;\boldsymbol{T}\,J_c\,d\xi.\quad (51)$$

The stiffness matrix $\boldsymbol{K}$ is calculated in the usual way.
$\boldsymbol{H}$ is calculated by assembling the elementary matrices $\boldsymbol{H}_e$ which satisfy

$$\boldsymbol{U}_e^{*T}\,\boldsymbol{H}_e\,\boldsymbol{dZ}_e=\int_{\hat{\Gamma}_e^c}[\![\boldsymbol{u}^*]\!]^T\boldsymbol{dt}\,J_c\,d\xi.\quad (52)$$

Consequently, one has

$$\boldsymbol{H}_e=\int_{\hat{\Gamma}_e^c}\boldsymbol{T}^T\boldsymbol{P}^T\boldsymbol{C}^T\boldsymbol{E}\,J_c\,d\xi.\quad (53)$$

Concerning the behavior of the cohesive zone, the compliance matrix $\boldsymbol{L}$ is defined such that if the test field $\boldsymbol{u}^*$ is equal to zero, then Eq. (41) takes the discrete and incremental form

$$\boldsymbol{Z}^{*T}\boldsymbol{H}^T\boldsymbol{dU}-\boldsymbol{Z}^{*T}\boldsymbol{L}\,\boldsymbol{dZ}=0,\quad \forall\,\boldsymbol{Z}^{*}\in\bar{G},\quad (54)$$

where $\bar{G}$ denotes the set of the column vectors of dimension $2\,m$. Matrix $\boldsymbol{L}$ is obtained by assembling the matrices $\boldsymbol{L}_e$ which satisfy

$$\boldsymbol{L}_e=\int_{\hat{\Gamma}_e^c}\boldsymbol{E}^T\boldsymbol{M}\,\boldsymbol{E}\,J_c\,d\xi,\quad (55)$$

where $\boldsymbol{M}$ is the tangent operator defined as

$$\boldsymbol{d}[\![\boldsymbol{u}]\!]=\boldsymbol{M}\,\boldsymbol{d\zeta}.\quad (56)$$

Equations (49) and (54) lead to the following global system of equations:

$$\begin{bmatrix}\boldsymbol{K}-\boldsymbol{J} & \boldsymbol{H}\\ \boldsymbol{H}^T & -\boldsymbol{L}\end{bmatrix}\begin{bmatrix}\boldsymbol{dU}\\ \boldsymbol{dZ}\end{bmatrix}=\begin{bmatrix}\boldsymbol{dF}_{ext}\\ 0\end{bmatrix}.\quad (57)$$

The iterative-incremental approach used for the numerical implementation and the corresponding algorithms are presented in Appendix B.

4.4 Test example B

This test example refers to the same geometry, boundary conditions and discretizations as test example A. The continuous material is also the same (elastic, isotropic, $E = 40\,\text{GPa}$,

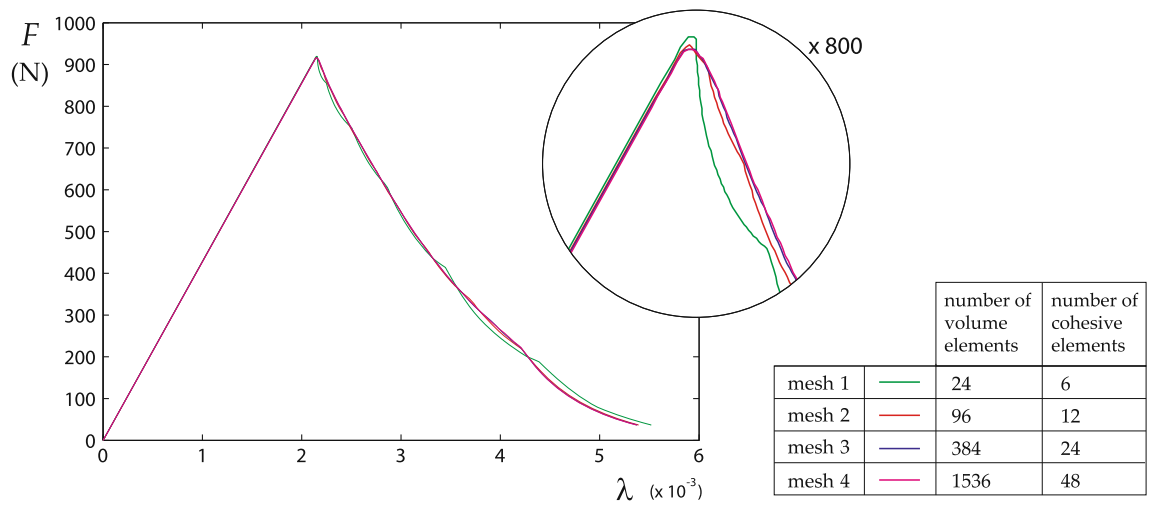

	number of volume elements	number of cohesive elements
mesh 1	24	6
mesh 2	96	12
mesh 3	384	24
mesh 4	1536	48

Fig. 10 Test example B: superposition of the loading curves obtained with all the meshes

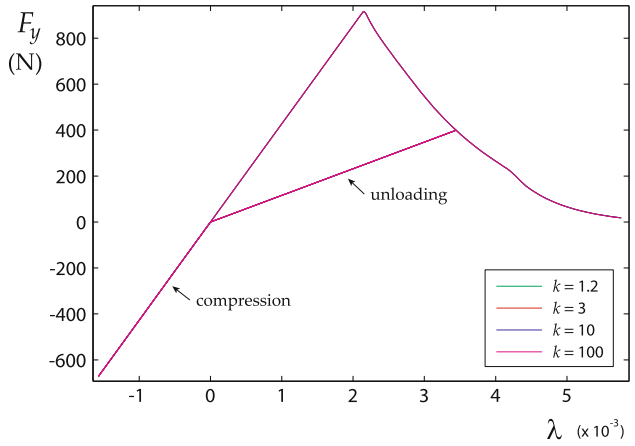

Fig. 11 Test example B: superposition of the loading curves obtained for the 4 values of k using mesh 4

$\nu = 0.2$) and plane stress conditions are assumed. Contrary to test example A, however, this test example uses the quadratic cohesive law presented in Sect. 4.1 in order to show the capability of the modified Lagrangian formulation to deal with broken cohesive elements (see the parameters in Sect. 4.1). The numerical parameter α was chosen according to Eq. (30) with $k = 3$, which led to $\alpha = 600$. Figure 10 shows the resulting force F applied to segment $[CD]$ as a function of loading factor λ for all the meshes. As in the case of test example A, the loading curves converge when the mesh density increases. Another computation has been performed using the mesh 4 to show the ability of the proposed implementation to cope with different values of the numerical parameter α and with the unloading and the contact of the cohesive zone. α is computed according to Eq. (30) with $k = 1.2$, $k = 3$, $k = 10$, $k = 100$. Figure 11 shows the projection F_y of the resultant of the forces applied on the segment $[DC]$ on $\boldsymbol{e}_y$ versus the loading factor λ for the 4 values of k. One can observe that the 4 curves are superimposed, which is natural as the 4 calculations only differ by a change of variable in the weak formulation. On the other hand, before the convergence is reached for a loading step, the 4 calculations may behave differently because of the different values of α. Figure 12 shows the number of iterations required at each loading step to reach convergence. One can observe that the number of iterations it slightly larger for the lower values of k (the total number of iterations is 2,583 for $k = 1.2$, 2341 for $k = 3$, 2288 for $k = 10$, 2229 for $k = 100$). However, the differences are not huge in this case.

4.5 Test example C

In test examples A and B, cohesive elements were used for cracks with known paths along which the normal and tangential components t_n and t_s of the cohesive traction were assumed to be C_0-continuous. This assumption is valid only if the crack's path is not excessively curved. This section presents a test example for which cohesive elements were introduced at the interfaces between all the volume elements of the mesh. Thus, the crack's path was allowed to bend

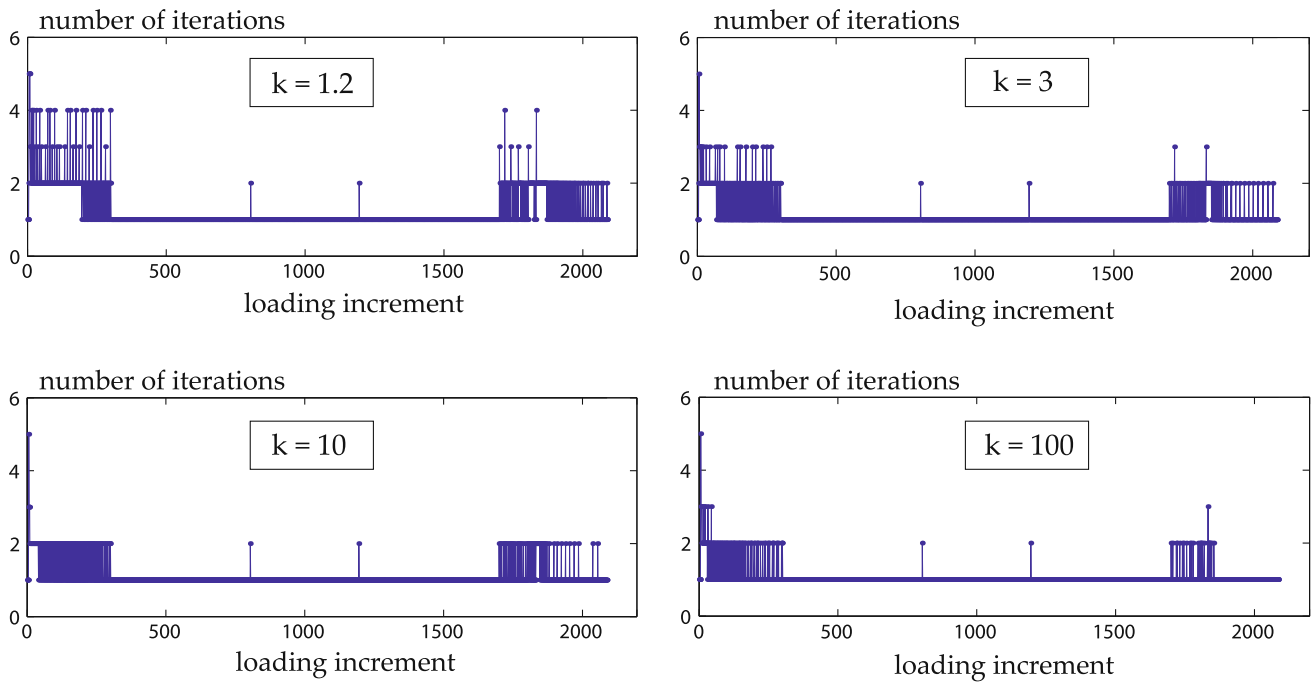

Fig. 12 Test example B: number of iterations at each loading step for 4 values of k

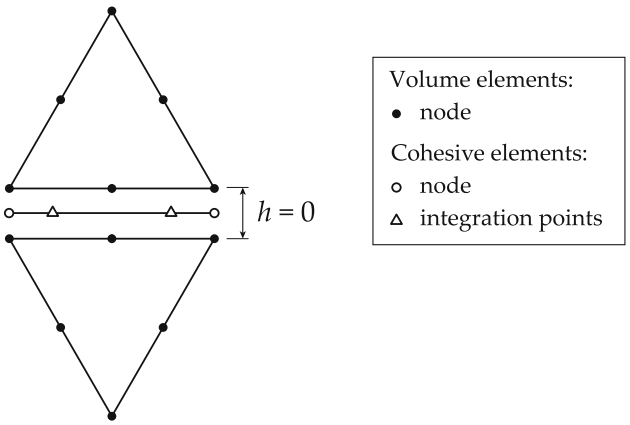

Fig. 13 Test example C: volume elements and cohesive elements

significantly and, consequently, the assumption of the continuity of the components of the cohesive traction was affected. Therefore, the following three modifications were made compared to test examples A and B:

- 6-node quadratic triangular elements instead of linear elements were used in the volume. Accordingly, the matrix of shape functions $\boldsymbol{C}$ of the cohesive elements was calculated using the quadratic displacement fields of the neighboring quadratic elements.
- The degrees of freedom of a cohesive element were considered to be independent of those of the neighboring cohesive elements (i.e. interelement continuity of the components of the cohesive traction was no longer assumed).
- Gauss points (instead of Newton-Cotes points for test examples A and B) were used for the numerical integration over the cohesive elements.

These modifications enable the proposed formulation to be used with kinks, irregular crack paths or branching cracks. Figure 13 shows the volume and cohesive elements used for test example C. Contrary to test examples A and B, these

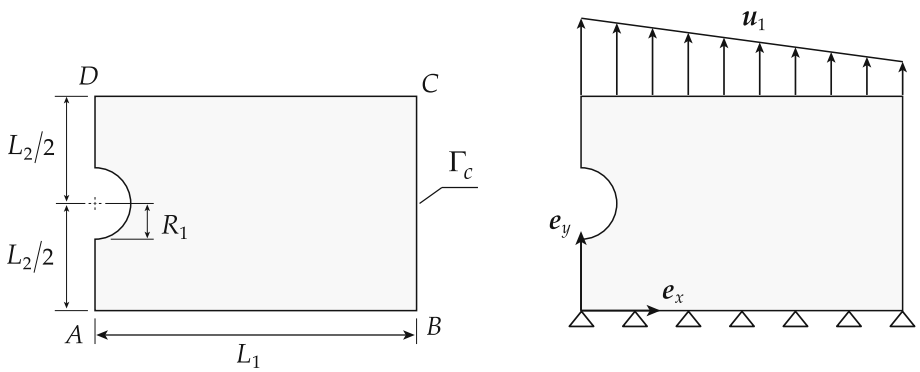

Fig. 14 Test example C: geometry and boundary conditions

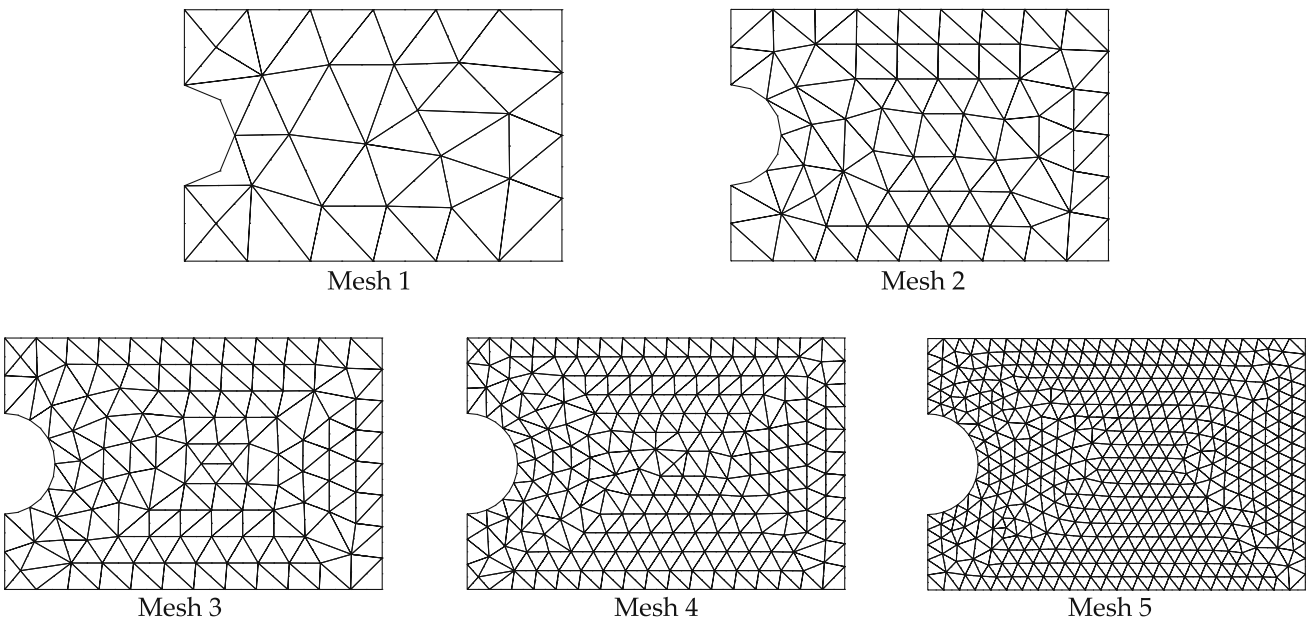

Fig. 15 Test example C: the five meshes used for the calculations

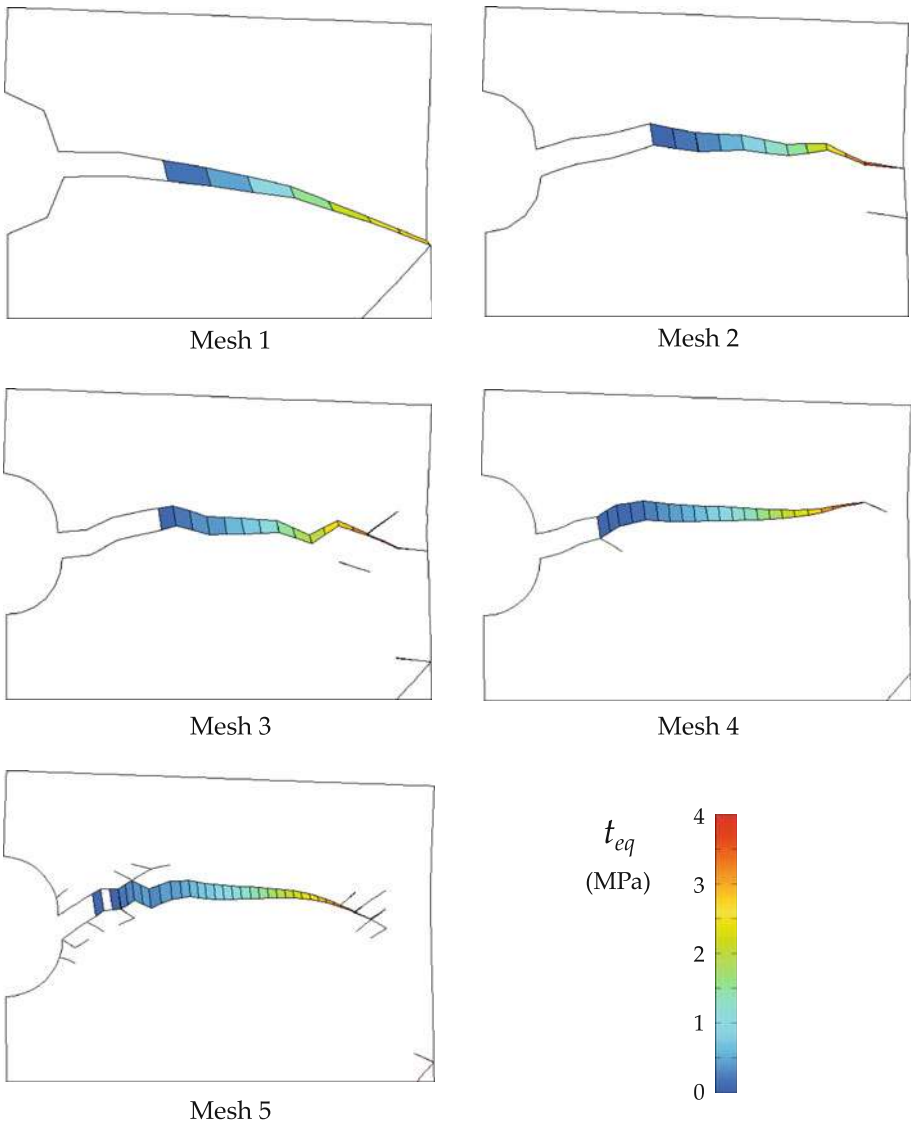

Fig. 16 Test example C: equivalent cohesive traction at load increment 1,200 (500× magnification)

volume elements were not compatible prior to crack initiation. Figure 14 shows the geometry of the structure and the boundary conditions used; these boundary conditions were the same as for test examples A and B. The geometric parameters were chosen to be $L_1 = 300$ mm, $L_2 = 200$ mm and $R_1 = 40$ mm. Figure 15 shows the five meshes used for the calculations; the density was multiplied by a factor $\sqrt{2}$ between each density level and the next. The continuous material was the same as for test examples A and B, and plane stress conditions were assumed. Similar to test example B, the calculations were based on the quadratic cohesive law of Sect. 4.1 using the modified Lagrangian formulation with the numerical parameter $\alpha = 600$. Figure 16 shows the equivalent cohesive traction t_{eq} plotted over the deformed structure after 1,200 load increments (out of $\approx$ 2,000). One should note that no stress oscillations were observed as a result of using Gaussian quadrature with the quadratic/linear approximation. Figure 17 shows the crack paths obtained for the different meshes at the end of the calculation. Figure 18 shows the loading curves corresponding to the different meshes. These are in relatively good agreement, although no real convergence can be observed because of the mesh dependency of the crack's path. From this test example, one can conclude that the modified Lagrangian formulation is capable of dealing with crack paths which are a priori unknown by using a quadratic/linear interpolation and introducing cohesive elements at the interfaces between all the volume elements of the mesh. One may wonder why the crack path is not stabilized with mesh 5. This is typical of this type of approach of crack propagation with CZM in which the crack path is forced to follow the edges of the volume elements. The method converges only with infinitely fine meshes.

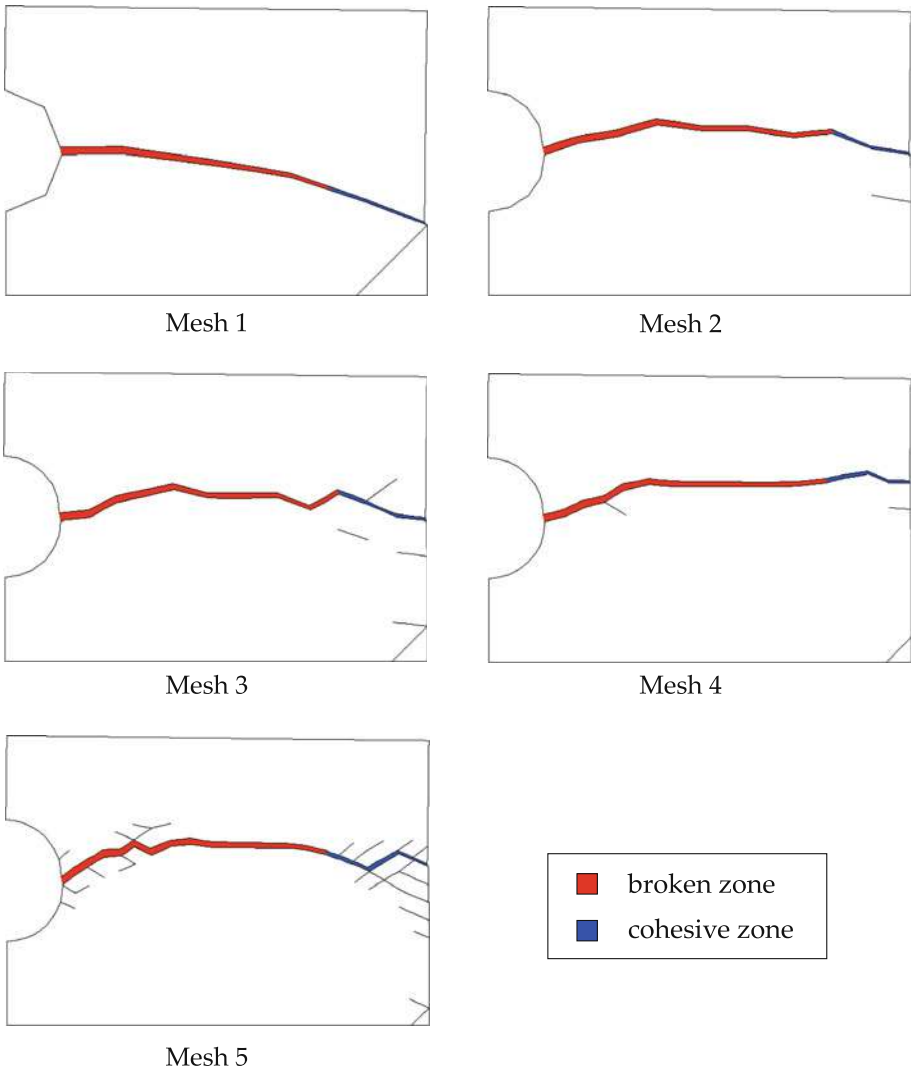

Fig. 17 Test example C: crack paths at the end of the computation for all the meshes (100× magnification)

5 Conclusion

In this paper, we presented a CZM based on an analogy with a smeared crack model which provides a relation between a parameter of the cohesive zone and the Poisson's ratio of the continuous material. This model was simulated using a two-field formulation capable of dealing with extrinsic cohesive laws, in which the field variables are the displacement over the continuous domain and the cohesive traction along the discontinuity. Contrary to standard displacement-based formulations, this Lagrangian formulation enables to cope with the infinite stiffness preceding the initiation of the cohesive elements. On the other hand, the Lagrangian formulation presents some difficulties in dealing with the fracture and the unloading of cohesive elements, which led to the development of the modified Lagrangian formulation in which, thanks to a change of variable, a fictitious cohesive traction is substituted for the cohesive traction in the weak equations of the mechanical problem. This change of variable also modifies the cohesive law, which becomes an increasing function of the displacement jump. The use of this increasing law provides an elegant way of dealing with the fracture and loading/unloading of cohesive elements. Both formulations were used to implement cohesive laws with standard linear volume elements and linear cohesive elements in the case of a straight crack propagation (test examples A and B). In this case, the cohesive elements are placed along the prescribed path of the crack and the approximate components of the cohesive traction are assumed to be continuous along this path. No oscillations of the calculated cohesive traction field were observed using Newton-Cotes integration points for the numerical integrations over the cohesive elements. Also, convergence of the global loading curve was observed as the mesh density increased. In test example C, the modified Lagrangian formulation was also used to simulate the propagation of a crack with an unknown path. In this example,

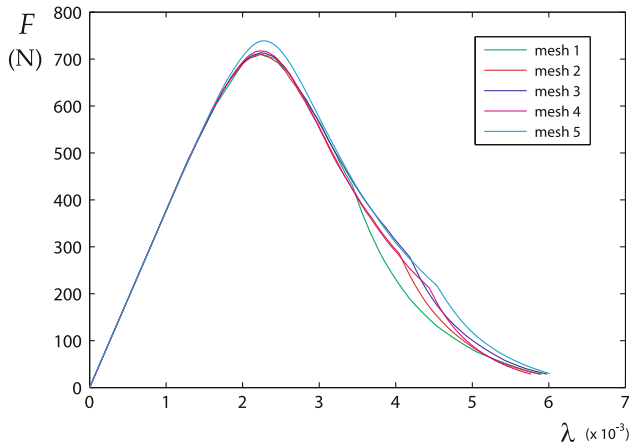

Fig. 18 Test example C: superposition of the loading curves for all the meshes

cohesive elements were placed at the interfaces between all the volume elements of the mesh; quadratic volume elements were used; interelement continuity of the components of the cohesive traction was not assumed; and Gauss points were used for the numerical integration over the cohesive zone. Again, no oscillations of the cohesive traction were observed. The loading curves did not converge as well as in the case of a straight crack because the crack's path is dependent upon the distribution of the volume elements in the mesh. This mesh dependency of the crack's path could be reduced by combining the proposed formulation with an Extended (X-FEM) or Embedded (E-FEM) Finite Element Method.

Acknowledgements This work was sponsored by the *SAFRAN* group (contract YHMMV 2007 012). Its support is gratefully acknowledged.

Appendix A: Thermodynamic of the CZM

This Appendix provides the thermodynamic equations of the CZM, justifying Eq. (16) linking the parameters γ and β of the model.

Thermodynamic potential The surface free energy potential, denoted ψ_c, is a function of $[\![\boldsymbol{u}]\!]$ and κ:

$$\psi_c = \psi_c([\![\boldsymbol{u}]\!], \kappa). \tag{58}$$

The dual potential $\psi_c^*(\boldsymbol{t}, \kappa)$, which is equal to the Legendre transform of ψ_c with respect to the displacement jump $[\![\boldsymbol{u}]\!]$, satisfies:

$$\psi_c^* = \psi_c - \boldsymbol{t}^T [\![\boldsymbol{u}]\!]. \tag{59}$$

According to [6], a surface dissipated energy increment $d\phi_c$ can be expressed as:

$$d\phi_c = \boldsymbol{t}^T \boldsymbol{d}[\![\boldsymbol{u}]\!] - d\psi_c, \tag{60}$$

and, according to (59):

$$d\phi_c = -[\![\boldsymbol{u}]\!]^T \boldsymbol{dt} - d\psi_c^*. \tag{61}$$

From the previous equation and the decomposition of $d\psi_c^*$ into

$$d\psi_c^* = \frac{\partial \psi_c^*}{\partial \boldsymbol{t}} \boldsymbol{dt} + \frac{\partial \psi_c^*}{\partial \kappa} d\kappa, \tag{62}$$

we obtain:

$$[\![\boldsymbol{u}]\!]^T = -\frac{\partial \psi_c^*}{\partial \boldsymbol{t}}, \tag{63}$$

$$d\phi_c = -\frac{\partial \psi_c^*}{\partial \kappa} d\kappa. \tag{64}$$

According to Eq. (3) which defines the displacement jump $[\![\boldsymbol{u}]\!]$, the potential ψ_c^* satisfies:

$$\psi_c^* = -\frac{1}{2} c_{eq}(\kappa)\, \boldsymbol{t}^T \boldsymbol{C}_0\, \boldsymbol{t}. \tag{65}$$

According to Eq. (65), the internal variable associated with κ, denoted $B = \partial \psi_c^* / \partial \kappa$, satisfies

$$B = -\frac{1}{2} \frac{\partial c_{eq}}{\partial \kappa}\, \boldsymbol{t}^T \boldsymbol{C}_0\, \boldsymbol{t}. \tag{66}$$

Consequently, Eq. (64) leads to

$$d\phi_c = \frac{1}{2} \frac{\partial c_{eq}}{\partial \kappa}\, \boldsymbol{t}^T \boldsymbol{C}_0\, \boldsymbol{t}\, d\kappa. \tag{67}$$

Path-independent dissipated energy It may be useful to define a surface free energy ψ_c which depends on κ alone because, then, the final surface dissipated energy is independent of the loading history. In order to do that, we enforce the following condition on the material parameters:

$$\gamma = \sqrt{\beta}. \tag{68}$$

Then, according to Eqs. (9) and (12), B satisfies

$$B = -\frac{1}{2} \frac{\partial c_{eq}}{\partial \kappa}\, t_{eq}^2. \tag{69}$$

The critical elastic energy release rate G_c, which is defined as the surface energy dissipated at a point of the crack throughout the decohesion process, is equal to:

$$G_c = \int_0^{[\![u]\!]_c} d\phi_c = \int_0^{[\![u]\!]_c} \frac{1}{2} \frac{\partial c_{eq}}{\partial \kappa}\, t_{eq}^2\, d\kappa, \tag{70}$$

where $[\![u]\!]_c$ is the equivalent displacement jump at rupture (which may be infinite). From Eq. (13), $c_{eq} = [\![u]\!]_{eq} / t_{eq}$ and, thus, if the cohesive law is in a loading state,

$$\frac{\partial c_{eq}}{\partial \kappa} = \frac{1}{t_{eq}} - \frac{\kappa}{t_{eq}^2} \frac{\partial t_{eq}}{\partial \kappa}. \tag{71}$$

Introducing the previous equation into (70), we obtain

$$G_c = \int_0^{[\![u]\!]_c} \frac{1}{2}\left(t_{eq}\, d\kappa - \kappa\, dt_{eq}\right). \tag{72}$$

This equation shows that if Eq. (68) is satisfied, then G_c is independent of the loading history and is equal to the area under the cohesive law (leading to t_{eq} as a function of $[\![u]\!]_{eq}$). This case reverts back to the definitions of the equivalent cohesive traction and of the equivalent displacement jump proposed in [32] (see also [33]). This assumption will be used in the remainder of the paper.

Appendix B: Implementation of the modified Lagrangian formulation

This Appendix provides the details of the iterative-incremental approach used for the implementation of the modified Lagrangian formulation and the corresponding algorithms.

The iterative-incremental approach In the first iteration, the calculation is performed by substituting in (57) the discrete increments $\boldsymbol{\delta U}$, $\boldsymbol{\delta Z}$ and $\boldsymbol{\Delta F}_{ext}$ for the infinitesimal increments $\boldsymbol{dU}$, $\boldsymbol{dZ}$ and $\boldsymbol{dF}_{ext}$:

$$\begin{bmatrix} \boldsymbol{K}-\boldsymbol{J} & \boldsymbol{H} \\ \boldsymbol{H}^T & -\boldsymbol{L} \end{bmatrix} \begin{bmatrix} \boldsymbol{\delta U} \\ \boldsymbol{\delta Z} \end{bmatrix} = \begin{bmatrix} \boldsymbol{\Delta F}_{ext} \\ 0 \end{bmatrix}. \tag{73}$$

From the weak Eq. (41), the residuals $\boldsymbol{R}_1$ and $\boldsymbol{R}_2$ are defined as

$$\boldsymbol{R}_1 = \boldsymbol{F}_{ext} + \boldsymbol{J}\,\boldsymbol{U} - \boldsymbol{H}\,\boldsymbol{Z} - \boldsymbol{F}_{int}, \tag{74a}$$

$$\boldsymbol{R}_2 = -\boldsymbol{H}^T\boldsymbol{U} + \boldsymbol{Y}, \tag{74b}$$

where $\boldsymbol{F}_{int}$ is calculated in the usual way and $\boldsymbol{Y}$ is calculated from the elementary vectors $\boldsymbol{Y}_e$ defined as:

$$\boldsymbol{Y}_e = \int_{\hat{\Gamma}_e^c} \boldsymbol{E}^T\, [\![\boldsymbol{u}]\!](\boldsymbol{\zeta})\, J_c\, d\xi. \tag{75}$$

The values of these residuals at iteration i are assumed to satisfy the linearized equations:

$$\boldsymbol{R}_1^i = \boldsymbol{R}_1^{i-1} - (\boldsymbol{K}-\boldsymbol{J})\boldsymbol{\delta U} - \boldsymbol{H}\,\boldsymbol{\delta Z}, \tag{76a}$$

$$\boldsymbol{R}_2^i = \boldsymbol{R}_2^{i-1} - \boldsymbol{H}^T\boldsymbol{\delta U} + \boldsymbol{L}\,\boldsymbol{\delta Z}. \tag{76b}$$

By enforcing that $\boldsymbol{R}_1^i$ and $\boldsymbol{R}_2^i$ in Eqs. (76a) and (76b) are equal to zero, we obtain

$$\begin{bmatrix} \boldsymbol{K}-\boldsymbol{J} & \boldsymbol{H} \\ \boldsymbol{H}^T & -\boldsymbol{L} \end{bmatrix} \begin{bmatrix} \boldsymbol{\delta U} \\ \boldsymbol{\delta Z} \end{bmatrix} = \begin{bmatrix} \boldsymbol{R}_1^{i-1} \\ \boldsymbol{R}_2^{i-1} \end{bmatrix}. \tag{77}$$

From this system of equations, the residuals $\boldsymbol{R}_1$ and $\boldsymbol{R}_2$ are minimized iteratively in the Newton algorithm until a prescribed error is reached.

Algorithms Algorithm 1 represents the global calculation procedure. I denotes the current loading step, I^{max} the final loading step, $(.)^{(I)}$ the converged value of a variable at step I, $(.)^i$ the value of a variable at iteration i of current step I, and IPs represent the integration points. Algorithm 2 represents the iterative calculation of the fictitious equivalent cohesive traction ζ_{eq} and of the other internal variables. For each integration point, $init$, $load$, c_0 and $rupt$ are the variables which provide the initiation state, the loading state, the contact state [according to Eq. (4)] and the fracture state respectively. The iterations are carried out until a residual res, which measures the gap between two successive values of ζ_{eq}, reaches a prescribed value. An advantage of the modified Lagrangian formulation which is illustrated in Fig. 19 is that one can easily distinguish a loading situation from an unloading situation by looking at the sign of the increment of variable ζ_{eq} between two loading steps.

Appendix C: Resolution of the systems of equations

The systems of equations resulting from the Lagrangian and the augmented Lagrangian formulations may be ill-conditioned because the orders of magnitude of the nonzero terms of the submatrices are different. Therefore, a change of variable is performed in order to improve the conditioning of the global matrix. Let us consider a system of the form:

$$\begin{bmatrix} \boldsymbol{K}_{11} & \boldsymbol{K}_{12} \\ \boldsymbol{K}_{21} & \boldsymbol{K}_{22} \end{bmatrix} \begin{bmatrix} \boldsymbol{X}_1 \\ \boldsymbol{X}_2 \end{bmatrix} = \begin{bmatrix} \boldsymbol{R}_1 \\ \boldsymbol{R}_2 \end{bmatrix}. \tag{78}$$

The change of variable is performed by solving the system

$$\begin{bmatrix} a_1 b_1\, \boldsymbol{K}_{11} & a_1 b_2\, \boldsymbol{K}_{12} \\ a_2 b_1\, \boldsymbol{K}_{21} & a_2 b_2\, \boldsymbol{K}_{22} \end{bmatrix} \begin{bmatrix} \boldsymbol{Y}_1 \\ \boldsymbol{Y}_2 \end{bmatrix} = \begin{bmatrix} a_1\, \boldsymbol{R}_1 \\ a_2\, \boldsymbol{R}_2 \end{bmatrix}, \tag{79}$$

with

$$\boldsymbol{X}_1 = b_1\, \boldsymbol{Y}_1, \tag{80a}$$

$$\boldsymbol{X}_2 = b_2\, \boldsymbol{Y}_2. \tag{80b}$$

Ideally, coefficients $a_1 b_1$, $a_1 b_2$, $a_2 b_1$, and $a_2 b_2$ should be set independently for each submatrix $\boldsymbol{K}_{ij}$. These coefficients, thereafter denoted γ_{ij}, are stored in a matrix $\boldsymbol{\gamma}$ which satisfies

$$\boldsymbol{\gamma} = \begin{bmatrix} \gamma_{11} & \gamma_{12} \\ \gamma_{21} & \gamma_{22} \end{bmatrix} = \begin{bmatrix} a_1 b_1 & a_1 b_2 \\ a_2 b_1 & a_2 b_2 \end{bmatrix}. \tag{81}$$

Since the determinant of $\boldsymbol{\gamma}$ is equal to zero, its components must satisfy

$$\gamma_{11}\,\gamma_{22} - \gamma_{12}\,\gamma_{21} = 0. \tag{82}$$

First, one calculates a matrix $\boldsymbol{\gamma}^*$ in which each coefficient γ_{ij}^* is equal to the inverse of the mean value of the nonzero terms of matrix $\boldsymbol{K}_{ij}$. Then, one calculates a matrix $\boldsymbol{\gamma}$ close

$I := 1$;
$\boldsymbol{U}^{(1)}$, $\boldsymbol{Z}^{(1)}$ and the vectors containing the strains, stresses, and internal variables are initialized to 0;
calculation of matrix $\boldsymbol{K}$;
while $I \leq I^{max}$ **do**
  $\boldsymbol{U}^0 := \boldsymbol{U}^{(I)}$;
  $\boldsymbol{Z}^0 := \boldsymbol{Z}^{(I)}$;
  $i := 1$;
  calculation of matrix $\boldsymbol{L}$;
  calculation of $\delta\lambda$;
  calculation of $\boldsymbol{\delta U}$ and $\boldsymbol{\delta Z}$;
  while *1 = 1* **do**
    $\boldsymbol{U}^i := \boldsymbol{U}^{i-1} + \boldsymbol{\delta U}$;
    $\boldsymbol{Z}^i := \boldsymbol{Z}^{i-1} + \boldsymbol{\delta Z}$;
    for *all the IPs in the volume,* **do**
      calculation of $\boldsymbol{\varepsilon}^i$ from $\boldsymbol{U}^i$;
      calculation of $\boldsymbol{\sigma}^i$ from $\boldsymbol{\varepsilon}^i$;
    end
    for *all the IPs at the interface* **do**
      calculation of $\boldsymbol{\zeta}^i$ from $\boldsymbol{Z}^i$;
      calculation of ζ_{eq}^i, $[\![\boldsymbol{u}]\!]^i$, $\boldsymbol{t}^i$, $init^i$, $load^i$, κ^i, c_0^i, and $rupt^i$ from $\boldsymbol{\zeta}^i$, $\zeta_{eq}^{(I)}$, $init^{(I)}$, $rupt^{(I)}$, and $\kappa^{(I)}$ (see Algorithm 2);
    end
    calculation of $\boldsymbol{R}_1^i$ from $\boldsymbol{\sigma}^i$;
    calculation of $\boldsymbol{R}_2^i$ from $[\![\boldsymbol{u}]\!]^i$;
    if *the errors are less than the tolerance,* **then**
      break;
    end
    updating of matrix $\boldsymbol{L}$;
    calculation of $\delta\lambda$;
    calculation of $\boldsymbol{\delta U}$ and $\boldsymbol{\delta Z}$;
    $i := i + 1$;
  end
  saving of $\boldsymbol{U}^{(I+1)}$, $\boldsymbol{Z}^{(I+1)}$ and the vectors containing the strains, stresses and internal variables;
  $I := I + 1$.
end

Algorithm 1: Modified Lagrangian formulation: global equilibrium

to $\boldsymbol{\gamma}^*$ and such that Eq. (82) is satisfied; the components of $\boldsymbol{\gamma}$ are calculated as:

$$\boldsymbol{\gamma}_{11} = \boldsymbol{\gamma}_{11}^* + \Delta\gamma^*, \tag{83a}$$
$$\boldsymbol{\gamma}_{22} = \boldsymbol{\gamma}_{22}^* + \Delta\gamma^*, \tag{83b}$$
$$\boldsymbol{\gamma}_{12} = \boldsymbol{\gamma}_{12}^* - \Delta\gamma^*, \tag{83c}$$
$$\boldsymbol{\gamma}_{21} = \boldsymbol{\gamma}_{21}^* - \Delta\gamma^*, \tag{83d}$$

with $\Delta\gamma^*$ defined as:

$$\Delta\gamma^* = \frac{\gamma_{12}^*\,\gamma_{21}^* - \gamma_{22}^*\,\gamma_{11}^*}{\gamma_{12}^* + \gamma_{21}^* + \gamma_{22}^* + \gamma_{11}^*}. \tag{84}$$

a_1 is chosen arbitrarily (e.g., $a_1 = 1$), and the remaining coefficients b_1, a_2, and b_2 are obtained from the relations $b_1 = \gamma_{11}/a_1$, $a_2 = \gamma_{21}/b_1$ and $b_2 = \gamma_{22}/a_2$.

Data: $\boldsymbol{\zeta}^i$, $\zeta_{eq}^{(I)}$, $init^{(I)}$, $rupt^{(I)}$, and $\kappa^{(I)}$;
$j := 1$;
calculation of $(\zeta_{eq})_j$ as a function of $\zeta_{eq}^{(I)}$ and $\delta\boldsymbol{\zeta}$ by linearizing the variation of ζ_{eq};
while $1 = 1$ **do**
  $init^i := \max\big(init^{(I)}, \arg((\zeta_{eq})_j > t_c)\big)$;
  $c_0^i := \arg(\zeta_n^i < 0)$;
  $rupt^i := \max\big(rupt^{(I)}, \arg\big((\zeta_{eq})_j > \alpha\,[\![u]\!]_c\big)$;
  if $init^i = 1$, **then**
    $load^i := \arg\big((\zeta_{eq})_j > \zeta_{eq}(\kappa^{(I)})\big)$;
    if $load^i = 1$, **then**
      calculation of $\kappa^i := [\![u]\!]_{eq}^i$ from ζ_{eq}^i;
    else
      $\kappa^i := \kappa^{(I)}$;
    end
    calculation of d_{eq}^i from κ^i and $rupt^i$;
    calculation of $[\![\boldsymbol{u}]\!]^i$ from d_{eq}^i, c_0^i and $\boldsymbol{\zeta}^i$;
    calculation of $\boldsymbol{t}^i$ from $[\![\boldsymbol{u}]\!]^i$ and $\boldsymbol{\zeta}^i$;
  else
    $[\![\boldsymbol{u}]\!]^i := \boldsymbol{0}$;
    $\boldsymbol{t}^i := \boldsymbol{\zeta}^i$;
    $\kappa^i := \kappa^{(I)}$;
    $c_0^i := 0$;
    $rupt^i := 0$;
  end
  calculation of $(\zeta_{eq})_{j+1}$ from $[\![\boldsymbol{u}]\!]^i$ and $\boldsymbol{t}^i$;
  $res := \big((\zeta_{eq})_{j+1} - (\zeta_{eq})_j\big)/(\zeta_{eq})_j$;
  if *res is less than the tolerance,* **then**
    break;
  end
  $j := j + 1$;
end
$(\zeta_{eq})^i := (\zeta_{eq})_j$;
Output: ζ_{eq}^i, $[\![\boldsymbol{u}]\!]^i$, $\boldsymbol{t}^i$, $init^i$, $load^i$, κ^i, c_0^i, and $rupt^i$

Algorithm 2: Modified Lagrangian formulation: updating of the internal variables

Appendix D: Cohesive elements

This section presents the shape functions and the rotation operators of the linear interface elements considered. $\boldsymbol{x}$ denotes the position vector of a point M of Γ_c, and x and y denote its projections onto $\boldsymbol{e}_x$ and $\boldsymbol{e}_y$:

$$\boldsymbol{x} = x\,\boldsymbol{e}_x + y\,\boldsymbol{e}_y. \tag{85}$$

The Jacobian J_c is defined by

$$d\Gamma_c = J_c\,d\xi, \tag{86}$$

where ξ is the curvilinear abscissa of a point of the reference cohesive element. Consequently, J_c satisfies

$$J_c = \sqrt{x_{,\xi}^2 + y_{,\xi}^2}\,. \tag{87}$$

Let $\boldsymbol{X}_{no}$ and $\boldsymbol{Y}_{no}$ denote the column vectors containing the coordinates of the nodes of the physical element. $\boldsymbol{N}$ is a line vector containing the shape functions which satisfy

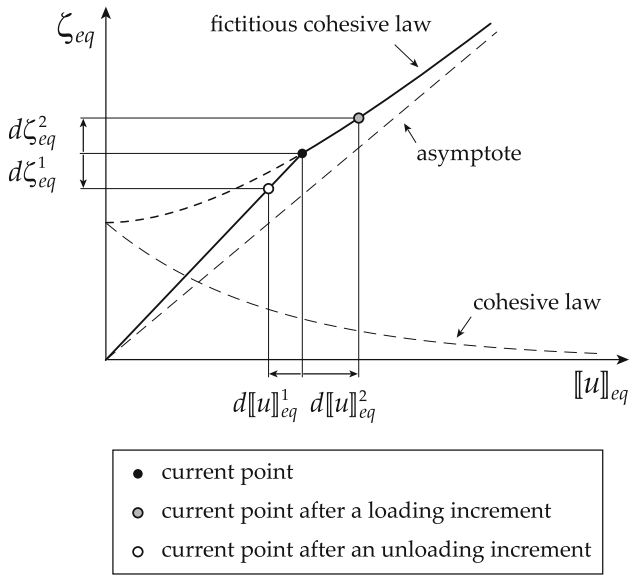

Fig. 19 Distinction between a loading state and an unloading state using the fictitious cohesive law

$$x(\xi) = \boldsymbol{N}(\xi)\, \boldsymbol{X}_{no}, \tag{88a}$$
$$y(\xi) = \boldsymbol{N}(\xi)\, \boldsymbol{Y}_{no}. \tag{88b}$$

The differentiation of these two equations with respect to ξ leads to the values of $x_{,\xi}$ and $y_{,\xi}$ used in the calculation of J_c [Eq. (87)]. The shape functions of the element are

$$N_1(\xi) = (1-\xi)/2, \tag{89a}$$
$$N_2(\xi) = (1+\xi)/2. \tag{89b}$$

The rotation matrix $\boldsymbol{P}$ is calculated as follows:

$$\boldsymbol{P}(\xi) = \begin{bmatrix} n_x & n_y & 0 & 0 \\ -n_y & n_x & 0 & 0 \\ 0 & 0 & n_x & n_y \\ 0 & 0 & -n_y & n_x \end{bmatrix}, \tag{90}$$

where n_x and n_y are the coordinates of the unit vector normal to the cohesive element in the $(\boldsymbol{e}_x,\boldsymbol{e}_y)$ basis, which satisfy

$$n_x = -\,y_{,\xi}\,/\,J_c\,, \tag{91a}$$
$$n_y = x_{,\xi}\,/\,J_c\,. \tag{91b}$$

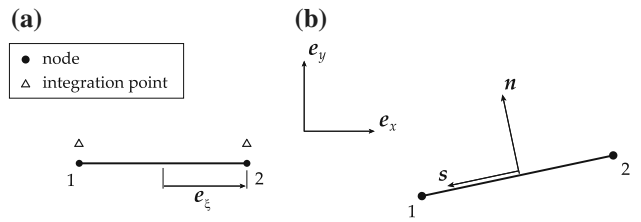

Fig. 20 Test examples A and B: **a** A reference element; **b** a physical element

Matrix $\boldsymbol{E}$ satisfies

$$\boldsymbol{E}(\xi) = \begin{bmatrix} N_1 & 0 & N_2 & 0 \\ 0 & N_1 & 0 & N_2 \end{bmatrix}. \tag{92}$$

If one uses linear volume elements (see test examples A and B and Fig. 20), matrix $\boldsymbol{C}$ is identical to matrix $\boldsymbol{E}$:

$$\boldsymbol{C}(\xi) = \begin{bmatrix} N_1 & 0 & N_2 & 0 \\ 0 & N_1 & 0 & N_2 \end{bmatrix}. \tag{93}$$

If one uses quadratic volume elements as in test example C and Fig. 21, a different sequencing of the nodes must be used for the approximation of the displacement jump and the calculation of matrix $\boldsymbol{C}$. In this case, matrix $\boldsymbol{E}$ is the same as if linear volume elements were used [Eq. (92)], but matrix $\boldsymbol{P}$ is recast as a matrix of dimension 6×6, and matrix $\boldsymbol{C}$ is modified to

$$\boldsymbol{C}(\xi) = \begin{bmatrix} N_1^q & 0 & N_2^q & 0 & N_3^q & 0 \\ 0 & N_1^q & 0 & N_2^q & 0 & N_3^q \end{bmatrix}, \tag{94}$$

with,

$$N_1^q(\xi) = \frac{1}{2}\,(\xi-1)\,\xi, \tag{95a}$$
$$N_2^q(\xi) = (1+\xi)\,(1-\xi), \tag{95b}$$
$$N_3^q(\xi) = \frac{1}{2}\,(\xi+1)\,\xi. \tag{95c}$$

Appendix E: Connection of the formulations proposed with mixed formulations

From the definition provided in [36], a mixed formulation leads to the resolution of a system of equations of the form

$$\begin{bmatrix} \boldsymbol{A} & \boldsymbol{B}^T \\ \boldsymbol{B} & \boldsymbol{0} \end{bmatrix} \begin{bmatrix} \boldsymbol{X}_1 \\ \boldsymbol{X}_2 \end{bmatrix} = \begin{bmatrix} \boldsymbol{F}_1 \\ \boldsymbol{F}_2 \end{bmatrix}. \tag{96}$$

Neither the modified Lagrangian formulation nor the Lagrangian formulation is a true mixed formulation because no matrix is equal to zero in the expression of Systems (73) and (77). However, one should note that if zero terms appear on the diagonal of matrix $\boldsymbol{L}$ the system of equations can be recast into the form of Eq. (96), which leads to a mixed formulation. This occurs if there remain cohesive elements which are not initiated. In particular, prior to initiating the first cohesive element, all the terms of matrix $\boldsymbol{L}$ are equal to zero. This must be taken into account in the implementation because, in order to ensure the stability of the numerical calculations, the mixed formulations must satisfy the *inf-sup* condition [24,25,37]. In particular, one can show that if $\boldsymbol{B}^T$ [with the notations of Eq. (96)] or $\boldsymbol{H}$ (for the two-field formulations presented) is not injective, then the *inf-sup* condition is not satisfied. Figure 22 shows an example of this situation in the case of a mesh consisting of two linear cohesive elements and two linear quadrilateral

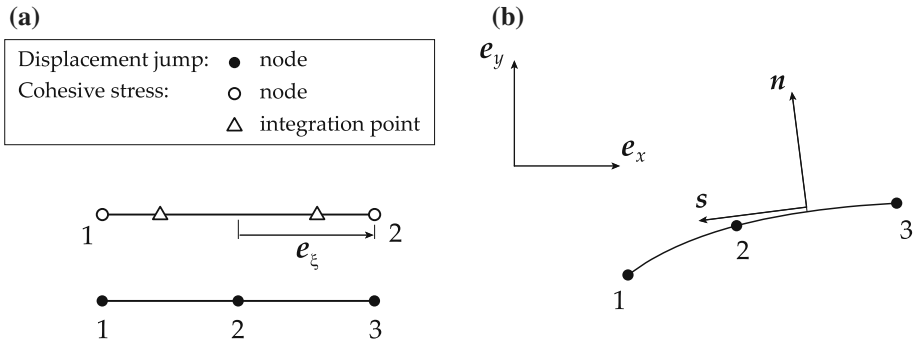

Fig. 21 Test example C: **a** A reference element; **b** a physical element

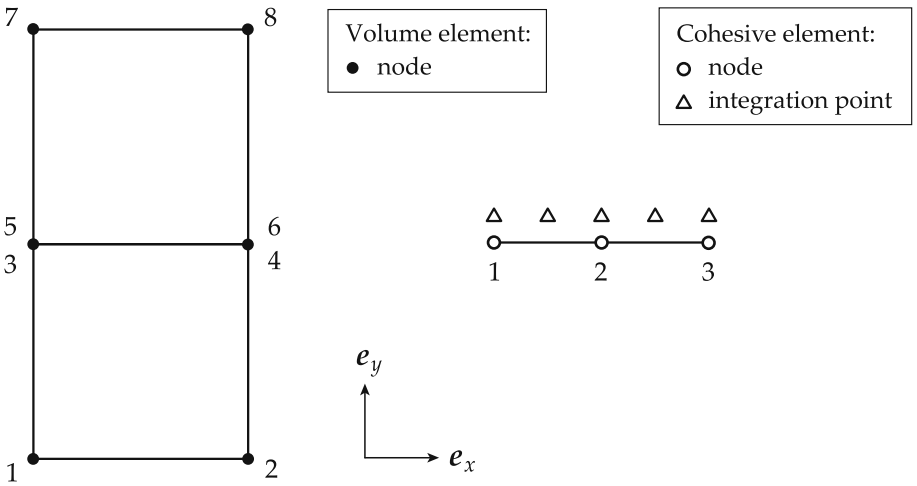

Fig. 22 Sample meshes of the continuous material and of the cohesive zone. When assembled, the cohesive element connects Nodes 3–5 and Nodes 4–6 of the volume elements

elements. If matrix $\boldsymbol{L}$ is equal to zero, the following three equations can be isolated from the global system of equations (using full integration in the case of this example):

$$\frac{5}{6}\left(u_5^y - u_3^y\right) + \frac{1}{6}\left(u_6^y - u_4^y\right) = 0, \tag{97a}$$

$$\left(u_5^y - u_3^y\right) + \left(u_6^y - u_4^y\right) = 0, \tag{97b}$$

$$\frac{1}{6}\left(u_5^y - u_3^y\right) + \frac{5}{6}\left(u_6^y - u_4^y\right) = 0. \tag{97c}$$

These three equations are linearly dependent because

$$(97a) + (97c) = (97b). \tag{98}$$

Consequently, the global matrix is not invertible. From this example, one can conclude that one should avoid using more degrees of freedom for the approximation of the cohesive traction $\boldsymbol{t}$ than for the calculation of the displacement jump $[\![\boldsymbol{u}]\!]$ along the sides of the crack.

References

1. Griffith A (1920) The phenomena of rupture and flow in solids. Philos Trans R Soc CCXXI(A):163–198
2. Barenblatt G (1959) Concerning equilibrium cracks forming during brittle fracture. The stability of isolated cracks. Relationships with energetic theories. PMM Appl Math Mech 23:1273–1282
3. Barenblatt G (1962) The Mathematical theory of equilibrium cracks in brittle fracture. Adv Appl Mech 7:55–129
4. Dugdale D (1960) Yielding of steel sheets containing slits. J Mech Phys Solids 8(2):100–108
5. Hillerborg A, Modéer M, Petersson P (1976) Analysis of crack formation and crack growth in concrete by means of fracture mechanics and finite elements. Cem Concr Res 6:773–782
6. Gurtin M (1979) Thermodynamics and the cohesive zone in fracture. Zeitschrift für Angewandte Mathematik und Physik (ZAMP) 30(6):991–1003
7. Petersson PE (1981) Crack growth and development of fracture zones in plain concrete and similar materials. Lund Institute of Technology, report TVBM-1006
8. Needleman A (1987) A continuum model for void nucleation by inclusion debonding. J Appl Mech (ASME) 54(3):525–531
9. Xu XP, Needleman A (1994) Numerical simulations of fast crack growth in brittle solids. J Mech Phys Solids 42(9):1397–1434
10. Simo J, Oliver J, Armero F (1993) An analysis of strong discontinuities induced by strain-softening in rate-independent inelastic solids. Comput Mech 12(5):277–296
11. Lofti H, Shing P (1995) Embedded representation of fracture in concrete with mixed finite elements. Int J Numer Methods Eng 38(8):1307–1325
12. Belytschko T, Black T (1999) Elastic crack growth in finite elements with minimal remeshing. Int J Numer Methods Eng 45(5):601–620
13. Moës N, Dolbow J, Belytschko T (1999) A finite element method for crack growth without remeshing. Int J Numer Methods Eng 46(1):131–150

14. Wells G, Sluys L (2001) A new method for modelling cohesive cracks using finite elements. Int J Numer Methods Eng 50(12):2667–2682
15. Wells G (2001) Discontinuous modelling of strain localisation and failure. Ph.D. thesis, Faculty of Aerospace Engineering and the Faculty of Civil Engineering and Geosciences, Delft University
16. Moës N, Belytschko T (2002) Extended finite element method for cohesive crack growth. Eng Fract Mech 69(7):813–833
17. Paggi M, Wriggers P (2012) Stiffness and strength of hierarchical polycrystalline materials with imperfect interfaces. J Mech Phys Solids 60(4):557–571
18. Charlotte M, Laverne J, Marigo JJ (2006) Initiation of cracks with cohesive force models: a variational approach. Eur J Mech A 25x(4): 649–669 (6th EUROMECH Solid Mechanics Conference)
19. Laverne J (2004) Formulation Énergétique de la Rupture par des Modèles de Forces Cohésives : Considérations Théoriques et Implantations Numériques. Ph.D. thesis, Université Paris XIII
20. Kubair D, Geubelle P (2003) Comparative analysis of extrinsic and intrinsic cohesive models of dynamic fracture. Int J Solids Struct 40(15):3853–3868
21. Lorentz E (2008) A mixed interface finite element for cohesive zone models. Comput Methods Appl Mech Eng 198(2):302–317
22. Bruggi M, Venini P (2007) A truly mixed approach for cohesive-crack propagation in functionally graded materials. Mech Adv Mater Struct 14(8):643–654
23. Bruggi M, Venini P (2009) Modeling cohesive crack growth via a truly-mixed formulation. Comput Methods Appl Mech Eng 198(47-48):3836–3851
24. Babuška I (1971) Error-bounds for finite element method. Numer Math 16(4):322–333
25. Babuška I (1973) The finite element method with Lagrangian multipliers. Numer Math 20(3):179–192
26. Johnson C, Mercier B (1978) Some equilibrium finite element methods for two-dimensional elasticity problems. Numer Math 30(1):103–116
27. Mergheim J, Kuhl E, Steinmann P (2004) A hybrid discontinuous Galerkin/interface method for the computational modelling of failure. Commun Numer Methods Eng 20(7):511–519
28. Elguedj T, Gravouil A, Combescure A (2007) A mixed augmented Lagrangian-extended finite element method for modelling elastic-plastic fatigue crack growth with unilateral contact. Int J Numer Methods Eng 71(13):1569–1597
29. Cazes F, Coret M, Combescure A (2010) Two fields formulations for the implementation of an extrinsic cohesive law. Civil-Comp Press, Valencia
30. Bažant Z, Oh B (1983) Crack band theory for fracture of concrete. Mater Struct 16(3):155–177
31. Paggi M, Wriggers P (2011) A nonlocal cohesive zone model for finite thickness interfaces—Part I: mathematical formulation and validation with molecular dynamics. Comput Mater Sci 50(5):1625–1633
32. Camacho G, Ortiz M (1996) Computational modelling of impact damage in brittle materials. Int J Solids Struct 33(20):2899–2938
33. Mariani S, Perego U (2003) Extended finite element method for quasi-brittle fracture. Int J Numer Methods Eng 58(1):103–126
34. Zienkiewicz O, Taylor R, Zhu J (2005) The finite element method: its basis and fundamentals, vol 1. Elsevier, Oxford, p 752
35. Schellekens J, de Borst R (1993) On the numerical integration of interface elements. Int J Numer Methods Eng 36(1):43–66
36. Auricchio F, Brezzi F, Lovadina C (2004) Encyclopedia of computational mechanics, 9-mixed finite element methods, vol 1. Wiley, New York
37. Brezzi F (1974) On the existence, uniqueness and approximation of saddle-point problems arising from Lagrangian multipliers. RAIRO Anal Numer 8(2):129–151